Polymer fiber waveguides for terahertz radiation

Nielsen, Kristian

Publication date:
2011

Document Version
Publisher's PDF, also known as Version of record

Polymer fiber waveguides for terahertz radiation

Kristian Nielsen

January 31st 2010

DTU Fotonik
Department of Photonics Engineering

DTU Fotonik
Department of Photonics Engineering
Technical University of Denmark
Ørsteds Plads 345V
DK-2800 Kgs. Lyngby
Denmark

Contents

Preface

The present thesis describes the scientific research carried out as part of my Ph.D. project in the period February 1st 2008–January 31st 2011.

The work took place at DTU Fotonik, Department of Photonics Engineering, Technical University of Denmark. The project was financed by the Technical University of Denmark and supervised by

- Ole Bang, Professor, DTU Fotonik, Technical University of Denmark, Kgs. Lyngby
- Peter Uhd Jepsen, Professor, DTU Fotonik, Technical University of Denmark, Kgs. Lyngby
- Henrik K. Rasmussen, Associate Professor, DTU Mekanik, Technical University of Denmark, Kgs. Lyngby

Acknowledgements

I would like to sincerely thank my supervisors for their support, help, suggestions, guidance, advice, and for making this project possible. A thanks has to go to Jesper Lægsgaard and Karste Rottwitt for always being available for discussions and having all the answers to dumb questions. A warm hearted thanks goes to our excellent mechanical workshop where Frank Persson, Jan N. Mortensen and Martin Nielsen make magic and are always willing to go the extra mile to help make the project move forwards. Their patience has been exemplary and their craftsmanship invaluable.

Workplace is empty without good colleagues and a thanks goes out to all my colleagues at DTU Fotonik. I must give a special thanks to my close colleagues Michael Frosz and Alessio Stefani, DTU Fotonik, for the countless discussions and ideas we've had together, and for sharing work's fun and frustrations. Their help in finishing this dissertation has heightened the level of presentation and comprehension. The biggest gratitude goes to my wife, Saima S. Nielsen, and our children for making getting up in the morning meaningful. My family and friends are invaluable in bringing balance to my life.

Kristian Nielsen, January 31st 2011

Abstract

Terahertz radiation offers many exciting applications noticeably in spectroscopy and it is showing promising results in imaging, mainly for security applications. In this project the study of using structured polymer fibers for THz waveguiding is presented. The inspiration for the THz fiber is taken from microstructured polymer optical fibers (mPOFs) used at optical wavelengths for sensing and communication. The fibers investigated can be divided into two groups, the solid core fibers and the hollow core fibers. The solid core fibers offer the broadest bandwidth with the best dispersion profile, while the hollow core fibers hold the promise for lowest loss but at the cost of lower bandwidth. In both cases the fabrication and characterization of the fibers is presented. The fibers are also investigated numerically and the numerical results are held up against the experimental results. The polymer material with lowest loss is Topas and all the solid core fibers are manufactured using this material. The polymer PMMA however has higher refractive index along with higher loss, and this higher refractive index is utilized to achieve a large bandwidth hollow core fiber with a low air-fill fraction. Finally, an example of an application is presented in the form of a broadband 3-dB directional fiber coupler. The device is numerically investigated and designed in such a way that it is manufacturable.

Resumé (Danish abstract)

Terahertz stråling tilbyder mange spændende applikationer specielt indenfor spektroskopi og viser også lovende resultater indenfor THz fotografi, med fokus på anvendelser indenfor sikkerhed. I dette projekt undersøges brugen af strukturerede polymer fibre til anvendelse som THz bølgeledere. Inspirationen til THz fiber kommer fra mPOF der bruges ved optiske bølgelængder til sensorer og kommunikation. De undersøgte fibre kan inddeles i to grupper: fastkerne fiber og hulkerne fiber. Fastkerne fiberen har den bredeste båndbredde og den bedste dispersionsprofil, mens hulkerne fiberen har potentiale for det laveste tab, men på bekostning af lavere båndbredde. Fremstilling og karakterisering af fibrene præsenteres. Fibrene undersøges også teoretisk og de beregnede resultater holdes op imod de eksperimentelle resultater. Alle fastkerne fibrene er lavet af Topas, da dette materiale har det laveste tab. Hulkerne fibrene er lavet af enten Topas eller PMMA; PMMA har højere tab end Topas men også højere brydningsindex. Dette kan udnyttes til at opnå en bredbåndet hulkerne fiber, ved lavere luftfyldningsforhold end hvad der er normalt ved telekom bølgelængder. Til sidst gives et eksempel på en bredbåndet 3-dB fiberkobler. Kobleren er teoretisk undersøgt og udformet på en sådan måde at den er realiserbar.

List of publications

The following publications form the basis of the present thesis:

Journal publications

[1] K. Nielsen, A. J. L. Adam, P. C. M. Planken, H. K. Rasmussen, O. Bang, P. U. Jepsen, "Bendable, low-loss topas fibers for the terahertz frequency range," Opt. Express **17**, 10, 8592-8601 (2009).

[2] K. Nielsen, H. K. Rasmussen, P. U. Jepsen, and O. Bang, "Broadband teraherz fiber directional coupler," Opt. Lett. **35**(17), 2879-2881 (2010).

[3] K. Nielsen, P. U. Jepsen, and O. Bang, "Porous core honeycomb band gap THz fiber," Accepted for publication in Opt. Lett. (2011).

Conference contributions

- K. Nielsen, H. K. Rasmussen, A. J. L. Adam, P. C. M. Planken, P. U. Jepsen, and O. Bang, "Dispersion-tailored, low-loss photonic crystal fibers for the THz range," in *Optical Terahertz Science and Technology Conference (OTST)*, Santa Barbara, USA 2009).

- K. Nielsen, H. K. Rasmussen, A. J. L. Adam, P. C. M. Planken, P. U. Jepsen, and O. Bang, "Low-loss and bendable THz fiber with tailored dispersion," in *Conference on Lasers and Electro-Optics*, Baltimore, USA (2009).

- K. Nielsen, O. Bang, and P. U. Jepsen, "Polymer microstructured Fibers for guiding of THz radiation," in *2010 Asia-Pacific Radio Science Conference (AP-RASC'10)*, Toyama, Japan (2010).

- K. Nielsen, H. K. Rasmussen, O. Bang, and P. U. Jepsen, "Broadband polymer microstructured THz fiber coupler with downdoped cores", in *International Conference on Infrared, Millimeter, and Terahertz Waves (IRMMW-THz)*, Rome, Italy (2010).

In addition, the following work was published during the Ph.D. project, but is outside the scope of the thesis:

Journal publications

- I. Johnson, W. Yuan, A. Stefani, K. Nielsen, H.K. Rasmussen, L. Khan, D. J. Webb, K. Kalli, and O. Bang, "Optical fibre Bragg grating recorded in TOPAS cyclic olefin copolymer," Electronics Letters, **47**, 3 (2011).

- A. Stefani, K. Nielsen, and O. Bang "Cleaving of Topas microstructured optical fibers," to be submitted.

- H. Pakarzadeh, K. Nielsen, A. C. Brunetti, K. Rottwitt, and A. Zakery "Raman spectra of PMMA-based microstructured optical fibers and direct measurement of their gain coefficient," to be submitted.

Conference contributions

- D. Cooke, K. Iwaszczuk, K. Nielsen, O. Bang and P. U. Jepsen, "Broadband THz waveguiding and high-precision broadband time-resolved spectroscopy : [invited]," *International Workshop on Terahertz Technology (TeraTech)*, Osaka, Japan (2009).

- M. H. Frosz, K. Nielsen, P. Hlubina, A. Stefani, and O. Bang, "Dispersion-engineered and highly-nonlinear microstructured polymer optical fibres," in *SPIE Europe Optics + Optoelectronics* , Prague, Czech Republic (2009)).

- L. Wei, T. T. Alkeskjold, S. U. Keller, J. M. Lindhard, H. V. Jensen, K. Nielsen, A. Boisen, and A. O. Bjarklev, "Compact Electrically tunable Waveplate Based on Liquid Crystal Photonic Bandgap Fibers," in *The Conference on Lasers and Electro Optics and the Quantum Electronics and Laser Science conference (CLEO/QELS)*, Baltimore, USA, (2009).

- P. Hlubina, D. Ciprian, M. H. Frosz, and K. Nielsen, "Measurement of chromatic dispersion of microstructured polymer fibers by white-light spectral interferometry," *SPIE Europe Optical Metrology*, Munich, Germany (2009).

- K. Nielsen, A. C. Brunetti, H. Pakarzadeh, and K. Rottwitt, "Stimulated Raman scattering in microstructured polymer optical fibers," *Photonics Europe, Photonic Crystal Fibers IV*, Brussels, Belgium (2010).

- I. Johnson, D. J. Webb, K. Kalli, W. Yuan, A. Stefani, K. Nielsen, H.K. Rasmussen, and O. Bang, "Polymer PCF grating sensors based on poly(methyl methacrylate) and TOPAS cyclic olefin copolymer," *SPIE Optics + Optoelectronics*, Prague, Czech Republic (2011).

- M.K. Szczurowski, O. Frazao, J.M. Baptista, K. Nielsen, O. Bang, and W. Urbanczyk, "Sensing characteristics of birefringent microstructured polymer optical fiber," *OFS-21, 21st International Conference on Optical Fiber Sensors*, Ottawa, Canada (2011).
- W. Yuan, A. Stefani, K. Nielsen, H. K. Rasmussen, D. J. Webb, K. Kalli, and O. Bang, "870nm Bragg grating in single mode TOPAS microstructured polymer optical fibre," *OFS-21, 21st International Conference on Optical Fiber Sensors*, Ottawa, Canada (2011).

Chapter 1

Introduction

1.1 Brief introduction to THz

Terahertz radiation is commonly defined as the electromagnetic oscillation range with a frequency between 100 GHz (10^9) and 100 THz (10^{12}) or equivalently the wavelengths ranging from 3 mm to 3 μm. In the radiation spectrum it lies between microwaves and the far-infrared, or between electronics and optics, as microwaves mark the upper frequency limit of electronics, and the far-infrared marks the lower frequency limit of optics. With the advent of new efficient sources and detectors and due to its unique possibilities in spectroscopy and imaging, terahertz (THz) radiation has attracted widespread attention in recent years [4].

At THz frequencies electromagnetic radiation interacts strongly with systems that have characteristic lifetimes in the picosecond range and/or energies in the meV range. Examples of such systems include bound electrical charges [5], free charge plasmas [6], strongly confined charge plasmas [7], transient molecular dipoles [8], phonons in crystalline solids [9], hydrogen bonds in chemicals [10], intermolecular forces in liquids [11], and biological matter [12].

The use of THz in imaging, possibly in conjunction with its spectroscopic qualities, has allowed for systems that can probe through cloths [13], wood [14] and plastics [15]. Since the THz radiation is very low energy radiation it will not damage the subject under investigation and it is completely harmless to humans. These qualities are being introduced and utilized in airport security and have obvious application in other explosive detection security areas [16].

The strong drive for exploration of the THz region in many fields of natural sciences has advanced the field of THz photonics. Parallel to the impressive development of THz sources and detectors there has also been significant development of new concepts for guided propagation of THz fields. Examples include dispersive propagation in square and circular metallic wave-

guides [17] and in plastic ribbon waveguides [19], dispersion-less propagation in parallel-plate waveguides [20] and in metallic ribbon waveguides [21], dispersion-less broadband THz wave propagation on thin metallic wires [22], weak guiding in polymer wires, TE-propagation in planar dielectric waveguides, and metallized glass tubes [23].

Consequently there are now several demonstrated THz-frequency waveguide concepts [1, 17, 19–28].

The main problem for THz waveguides is attenuation: material loss, scattering loss and confinement loss. Then, depending on the application, the second problem is dispersion. In applications where continuous radiation sources are used, dispersion is not a big problem, but when THz pulses are used in the application, managing dispersion becomes a problem.

Apart from metallic and glass waveguides [23, 29], the material of choice when making THz waveguides is polymer: e.g. poly(methyl-methacrylate) (PMMA) [30], Teflon [31], high density polyethylene (HDPE) [24, 32] and Topas [1]. The reasons for this material choice are that polymers have the lowest loss of most materials in the THz range and they are for the most part easy to machine.

In both spectroscopy and imaging, the use of THz waveguides can be very beneficial. In spectroscopy, waveguides have traditionally been applied to increase sensitivity as they increase the overlap of radiation and sample. Waveguides can also be applied to probe materials that have too high absorbtion to be effectively analyzed using transmission or reflection, in this case the evanescent tail of the confined radiation can be made to overlap with the sample over an increased interaction length. In imaging, the waveguide can be utilized in the same manner as an optical fiber is utilized in an endoscope. In both cases the detector is either too bulky or too sensitive to be moved around to make an image of the sample, here a flexible waveguide could scan the sample and transmit the image of the sample to the detector, pixel by pixel.

1.2 Scope of thesis

The purpose of this Ph.D. project was to manufacture and apply structured polymer fibers as THz waveguides. The inspiration for the THz fibers is found in traditional photonic crystal fibers (PCFs), either based on silica or polymer. The advantage of using PCFs is that they offer the ability to manufacture fibers with large variation in loss and dispersion characteristics. As any other fiber the THz fibers should have low loss. The best way to achieve low loss is to use a material with inherently low loss. In the THz range, of all the different solid dielectric materials, specific polymers offer the lowest material loss. For a polymer to have low loss it must be non-polar. This is necessary as any polarity will start to oscillate when an oscillating

electro-magnetic field is applied, and thereby absorb power. The THz fibers have been studied numerically to determine the expected characteristics. In these studies both a finite-difference and a finite-element mode solver have been used.

1.3 Organization of thesis

In chapter 2 the waveguide equations governing the waveguide design are explained along with the numerical tools necessary to solve them. The polymers used in this project are characterized, and different known waveguide designs are presented. Chapter 3 presents the manufacturing of the THz fibers, the fiber draw tower is presented along with the different draw parameters and considerations. In chapter 4 the terahertz time domain spectroscopy setups are described, as well as the optically switched conductive antenna that form the foundation of the setups. In chapters 5 and 6 the fabricated THz fibers are presented. Chapter 5 is devoted to the solid core fibers and chapter 6 is devoted to the hollow core fibers. The transmission measurements for the fibers are presented and the loss and dispersion are analyzed. Chapter 5 is split between the large mode area fiber and the small mode area fiber. Likewise, chapter 6 is split between the triangular cladding structure and the honeycomb cladding structure. In chapter 6 the subject of imaginary index guiding is introduced.

Chapter 7 will look at a THz fiber application, namely a novel broadband 3-dB directional fiber coupler.

In chapter 8 a summary will be given and then a conclusion with an outlook.

Chapter 2

Waveguide design

2.1 Waveguide theory

Maxwell's equations describe the behavior of electromagnetism.

$$\nabla \times \mathbf{E} = -\frac{\partial \mathbf{B}}{\partial t} \tag{2.1}$$

$$\nabla \times \mathbf{B} = \mathbf{J}_f + \frac{\partial \mathbf{D}}{\partial t} \tag{2.2}$$

$$\nabla \cdot \mathbf{B} = 0 \tag{2.3}$$

$$\nabla \cdot \mathbf{D} = -\rho_f \tag{2.4}$$

where $\mathbf{E}$ and $\mathbf{B}$ are the electric and magnetic field vectors respectively. The auxiliary dielectric and magnetizing fields, $\mathbf{D}$ and $\mathbf{H}$ respectively, are simple when working with linear non-magnetizable materials.

$$\mathbf{D} = \epsilon \mathbf{E} \tag{2.5}$$

$$\mathbf{H} = \frac{1}{\mu_0}\mathbf{H} \tag{2.6}$$

In the field of optics the material properties are usually given by the refractive index (n) and the absorbtion (α). Assuming that the absorption is negligible the relation is straight forward: $\epsilon = \mathrm{n}^2$. If the absorption can not be neglected the relation is more complicated. The material absorbtion has to be rewritten as κ and introduced into a complex refractive index: $\tilde{\mathrm{n}} = \mathrm{n} - i\kappa$ where $\kappa = \frac{\alpha c}{2\omega}$ and c is the speed of light in vacuum. The relation between refractive index, absorption and ϵ is: $\epsilon = \tilde{\mathrm{n}}^2 = \mathrm{n}^2 - \kappa^2 + 2\kappa \mathrm{n} i$.

A waveguide is a device that confines electromagnetic (EM) radiation in the transverse direction while transmitting it in the longitudinal direction. This can be achieved in different ways, the design of choice depends on

whether one used technology from the microwave community or from the optics community.

In the microwave community radiation has typically been confined to a dielectric trapped between two metals. In the optical community the confinement is usually achieved by modulating the refractive index of the transverse profile of the device.

In the waveguiding device the transverse distribution of the radiation is called a mode and the effective speed of the propagation in the longitude direction is called the propagation coefficient. These two properties are the eigenstate and the eigenvalue to the EM wave equation, a second order partial differential equation derived from Maxwell's equations. In the derivation it is assumed that there is no free charge and current, $\rho_f = 0$ and $\mathbf{J}_f = 0$, and the medium is linear and non-magnetizable. Applying the Curl operator $(\nabla\times)$ to both sides of Eqn. (2.1) we get:

$$\nabla \times \nabla \times \mathbf{E} = -\frac{\partial}{\partial t}\nabla \times \mathbf{B} = -\mu_0 \frac{\partial^2 \mathbf{D}}{\partial t^2} \tag{2.7}$$

using the vector identity:

$$\nabla \times (\nabla \times \mathbf{A}) = \nabla(\nabla \cdot (\mathbf{A})) - \nabla^{\mathbf{2}}\mathbf{A}$$

and since Eqn. (2.5) gives $\nabla \cdot \epsilon\mathbf{E} = 0$ and using the identity $\nabla \cdot \epsilon\mathbf{E} = \epsilon\nabla \cdot \mathbf{E} + \mathbf{E} \cdot \nabla\epsilon \Rightarrow \nabla \cdot \mathbf{E} = -\frac{1}{\epsilon}\nabla\epsilon \cdot \mathbf{E}$. We finally arrive at the wave equation.

$$\nabla^2\mathbf{E} - \frac{n^2}{c^2}\frac{\partial^2 \mathbf{E}}{\partial t^2} + \nabla\left(\frac{1}{\epsilon}\nabla\epsilon \cdot \mathbf{E}\right) = 0$$

Where $\frac{n^2}{c^2} = \mu_0\epsilon$, c is the speed of light in vacuum. If the refractive index modulation is small the last term on the left side of Eqn. (2.1) can be ignored and the wave equation reduces to the scalar wave equation and becomes substantially easier to solve. This approximation is not accurate when large refractive index shifts are involved but can even then offer some quantitative information [33].

For the solution of the wave equation it can be assume that it consists of a harmonically oscillating field component in the z-direction, with a frequency ω and a propagation coefficient β: $\mathbf{E} = \mathbf{E}(x, y)\exp(-i(\omega t + \beta z))$. There is no refractive index modulation in the z-direction. Putting this assumed solution into the wave equations, and using yet another vector product rule we get the coupled equations governing the distribution in the transverse direction:

$$(\nabla_{xy}^2 + \beta^2 - n^2k^2)E_x + \frac{1}{n^2}\frac{\partial(n^2)}{\partial y}\left[\frac{\partial E_y}{\partial x} - \frac{\partial E_x}{\partial y}\right] = 0 \tag{2.8}$$

$$(\nabla_{xy}^2 + \beta^2 - n^2k^2)E_y + \frac{1}{n^2}\frac{\partial(n^2)}{\partial x}\left[\frac{\partial E_x}{\partial y} - \frac{\partial E_y}{\partial x}\right] = 0 \tag{2.9}$$

These equations together with the appropriate boundary conditions have to be solved in order to calculated the field distribution inside the waveguide and also the effective refractice index of the waveguide given by $n_{\text{eff}} = \beta/k$. The frequency dependence of n_{eff} determines the dispersion of the waveguide.

2.2 Numerical modeling of THz fibers

The aim of the numerical study is to solve Maxwell's equations by assuming that the problem is of a transversal nature and that the longitudinal component is harmonically oscillating.

2.3 MIT Photonic Bands Package (MPB)

A useful and very popular numerical tool for modeling photonic crystal fibre (PCF) is the MIT Photonic Bands Package. It is based on the planar wave method [34] and works by solving the Hermitian eigenvalue problem that is found by following the same procedure as when finding Eqn. (2.7). Instead of applying the $\nabla\times$ operator on Eqn. (2.1) it is applied to Eqn. (2.2). Then transforming to frequency one gets Eqn. (2.10).

$$\nabla \times \frac{1}{\epsilon_r} \nabla \times \mathbf{H} = \frac{\omega^2}{c^2} \mathbf{H} \tag{2.10}$$

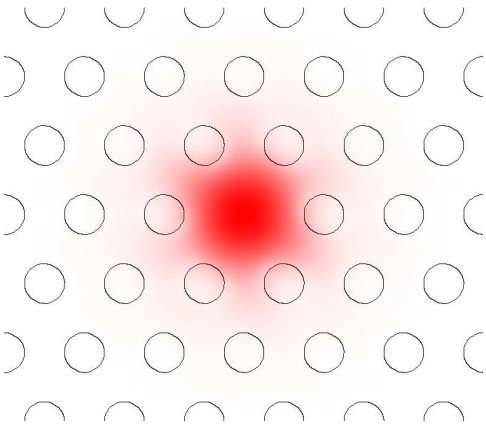

Figure 2.1: Example of a 6×6 super cell calculated mode using MPB.

The requirement for Eqn. (2.10) to be a Hermitian problem is that ϵ_r is real, which limits the applications of MPB to only loss-less waveguides. But this also includes low loss waveguides, as the error in assuming a loss-less medium is very small. MPB solves problems that have periodic structure.

The user must make sure that the structure complies to conditions of periodicity. The cladding of PCF is made of repeating unit cells, typically these unit cells are based on a triangular distribution of holes. The smallest unit cell is made of one hole and has the dimensions $\Lambda \times \frac{\sqrt{3}}{2}\Lambda$. One unit cell is enough when calculating the effective index of the cladding. When core mode calculations are needed the cell must be larger. The core is constructed by introducing defects in the cladding, removing holes. The calculation cell then consists of the defect together with the cladding. Because of the periodicity of the method the defects will also be repeated to infinity. In order to ensure that the defects do not couple, each calculation cell must be large enough to ensure that field component at the boundary is negligibly small. Typically when solving a one-hole defect core the calculation cell must consist of 6×6 unit cells. An example of such a calculation is given in Fig. 2.1.

2.4 Commercial mode solver (COMSOL)

The periodicity requirement of the MPB software together with the requirement of the refractive index to be real are limiting especially when dealing with THz waveguides. Firstly the waveguides are typically smaller than optical waveguides when scaled by wavelength, therefore the structure is not just a cladding with a defect, but rather has to take into account the thickness of the fiber and the limited extent of the cladding as well. Secondly since the material loss of most polymers in the THz range is large, it can not be neglected and must be included in the calculation, making the refractive index complex. For these reasons the commercial mode solving software called COMSOL has proven to be very useful. It can handle almost any structure, the refractive index can be complex, and it allows for means to reduce the calculation domain.

2.4.1 Perfectly matched layers

Ideally a calculation domain should extend to infinity. However this is not practical. One approximation to infinity is to make the calculation domain large enough that the assumption of zero field at the boundary is valid. This is the approach used in MPB. However large computational domains require large amounts of memory. Memory together with computational speed are the limiting factors of any numerical calculation. Early attempts at improving the computational domain included the introduction of an absorbing layer around the edges of the domain. All the early attempts suffered from reflection due to the abrupt changes in the refractive index profile. The introduction of the perfectly matched layer (PML) was the first absorbing layer that produces no reflection regardless of the incident angle. When modeling waveguides PML is used to reduce the calculation domain

but simultaneously the introduction of a PML in the calculation domain includes the confinement loss of the modes, allowing for the total loss of the proposed THz fiber to be calculated. The total loss consists of the confinement loss together with the absorption loss.

2.4.2 Symmetry reduction

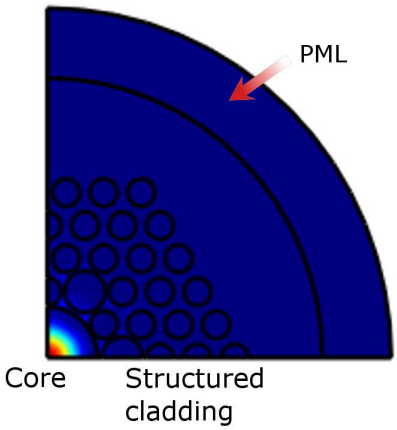

Figure 2.2: Example of a COMSOL calculation showing a mode in a hollow core structure.

Since the THz fibers are circular in the transverse plane with a four fold symmetry, the computational domain can be reduced to one quarter using appropriate boundary conditions. An example of this reduction is shown in Fig. 2.2 along with the calculated core mode. This reduction comes in very handy when it is only interesting to find the fundamental mode of a solid core fiber. The polarization of the mode is given by the boundary conditions. The boundary conditions are either a perfect electric conductor or a perfect magnetic conductor. When solving for the fundamental mode the boundaries must be of each type. However when performing calculations on hollow core fibers, where all the cladding modes need to be calculated, one needs to repeat the calculations four times, one time for each of the four boundary condition combination that can be made. This ensures that all the supported modes are found.

2.5 THz characteristics of polymers

If the waveguide design calls for a dielectric then for THz applications the best choice is dry air. Dry air has a refractive index of practically 1 and

almost no loss in the THz domain. However a waveguide can not comprise of air alone. The material best suited for manufacturing purely dielectric waveguides is polymer. The range of polymers available is large, however THz waveguide research focuses mainly on the low-loss polymers such as Teflon, Topas and HDPE. The refractive index and absorption of three low loss polymers is shown in Fig. 2.3, cyclic-olefin, Picarin and Topas are basically the same material.

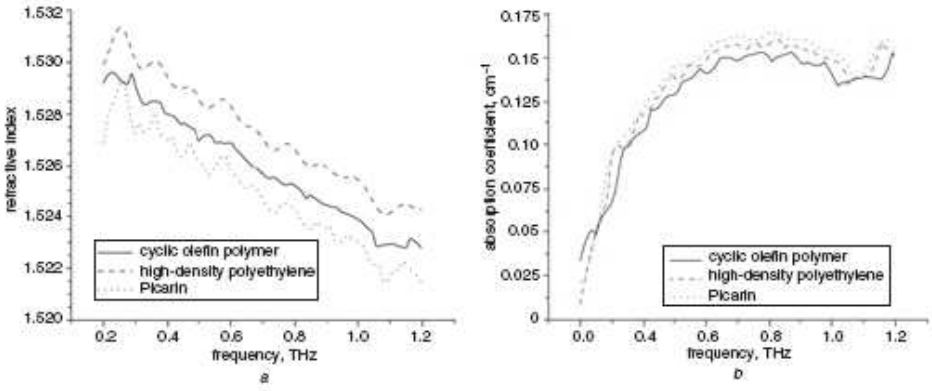

Figure 2.3: Refractive index (a) and loss (b) of three low loss polymers [35].

Compared to these three polymers other polymers have large losses as seen in Fig. 2.4. The one polymer of interest in this figure is poly(methyl-methacrylate) (PMMA) since it is also used in this project.

The polymers PMMA and Topas, which is a cyclic-olefin, can vary in composition of monomers depending on brand and fabrication process. This variation leads to different refractive indexes and absorption. Therefore the polymers used in this project, PMMA and Topas, are characterized using THz spectroscopy to determine exactly their properties in the THz range. The result of the spectroscopy is shown in Fig. 2.5. The samples used in this characterization are 2 cm thick, it is this thickness that limits the result to the low frequencies in the case of PMMA. The index of refraction of Topas is flat within the bandwidth of the system. The amorphous structure of Topas combined with the nonpolar polymer chains, assure this very low absorption and dispersion.

It is also notable that there is a break in the loss axis of Fig. 2.5(b) because the losses of PMMA are around 50 times higher than those of Topas. One other notable quality of Topas is that Topas as opposed to many other polymers, does not absorb water [36].

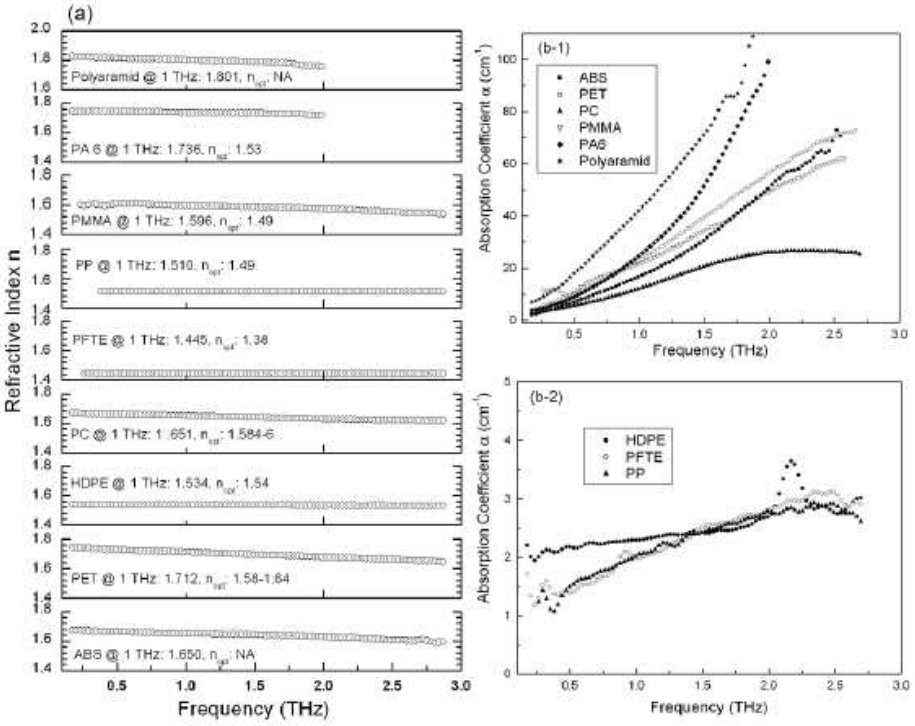

Figure 2.4: Refractive index (a) and loss (b) of nine different but common polymers [37]. All with attenuations higher than 1 cm^{-1}.

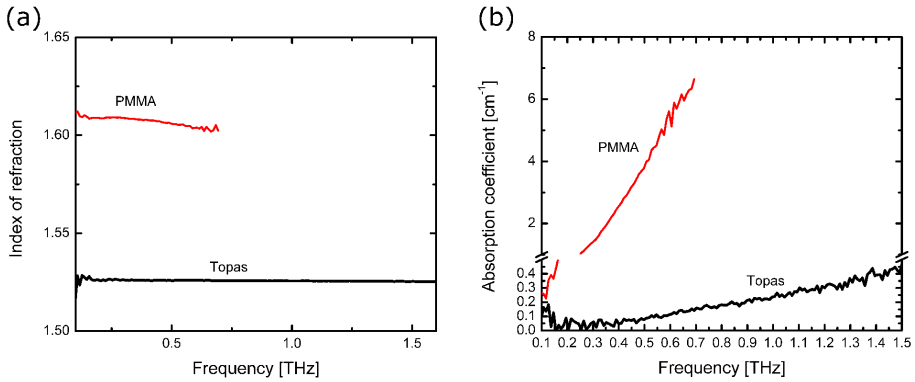

Figure 2.5: Refractive index (a) and loss (b) of the PMMA and Topas polymers used in this project.

2.6 State of the art of THz waveguides

Due to the relative ease of fabrication and the close analogy to guiding in optical fibers in the near infrared, optical fibers designed for the THz frequency range have attracted considerable attention. Silica glass has low absorption and low dispersion in the THz range when compared to other glass types [38]. However, compared to its properties at near-infrared wavelengths, the THz absorption is still too high for guiding over distances of practical relevance. Hence different types of polymers have been proposed and demonstrated as an alternative material for the fabrication of THz-frequency optical fibers.

The simplest polymer fiber is a step index fiber consisting of a core with a high refractive index and a cladding with a lower refractive index. Chen *et al.*[24] used a sub-wavelength polyethylene (PE) fiber suspended in air as a highly flexible and low-loss waveguide for THz radiation. The modal confinement in such a fibre is strongly frequency dependent, leading to significant dispersion and frequency-dependent losses. Handling and especially bending of such a thin fiber is difficult due to the low confinement of the propagating field inside the fiber, leaving the guided propagation susceptible to external disturbances. However, the propagation loss was demonstrated to be less than 0.05 dB/cm at 350 GHz, allowing propagation over long distances. The strong dispersive properties of sub-wavelength fibers were characterized by Jamison *et al.*[39].

An alternative approach is to use a PCF for the guiding which can then be achieved either by the photonic band gap effect or by the lower effective index of the microstructured cladding surrounding the core. A PCF designed for the THz range can have the same appealing properties as a PCF designed for the traditional near-infrared frequencies, for instance supporting single-mode propagation at any frequency [40]. Han *et al.*[32] demonstrated index-guided propagation with a loss lower than 2.2 dB/cm in a solid core of PE in a hexagonally stacked array of PE tubes fused together. Later Goto *et al.*[31] showed index-guiding with a loss of approximately 0.5 dB/cm in a teflon solid-core PCF, fabricated by stacking of teflon tubes.

Recently the use of polymer-based microstructured polymer optical fibers (mPOFs) for transmission of THz-frequency radiation has been suggested. Ponseca *et al.*[30] described a fabrication method where the hole pattern of the photonic crystal structure was drilled into a PMMA block which was then drawn down to a fiber of appropriate dimensions for THz guiding. Their fiber consisted of PMMA with an air core surrounded by circular rings of air holes acting as the low-index layers of a circular Bragg reflector. THz propagation with a loss in the range of 0.9-1.3 dB/cm was observed.

Propagation by the photonic band gap effect in air-core fibers has not been demonstrated experimentally in the THz frequency range yet, but was studied numerically by Geng *et al.*[41] and Vincetti [42] who calculated the

propagation loss and dispersion in polymer-based band gap fibers. Losses in the band gap in the range of 0.05 dB/cm together with relatively low dispersion showed that such fibers could be promising candidates for low-loss, narrow-band THz propagation.

Hassani *et al.*[43] recently proposed a novel guiding mechanism with high confinement of the guided mode in the core of an air-clad fiber, based on a distribution of sub-wavelength holes inside the core of the fiber. In their simulations, based on microstructured teflon cores, losses in the range of 0.1-0.5 dB/cm were predicted. The same guiding mechanism was proposed by Atakaramians *et al.*[25] and their simulations, based on microstructured PMMA cores, estimated the losses to be 1-2 dB/cm.

Currently there is much research invested in lowering the loss by forcing a large part of the radiation to propagate in air while still being confined to a waveguide, i.e. sub-wavelength fiber [24], porous fibers [25, 43] and hollow core fibers. Of these, the hollow core fiber is the least sensitive to outside perturbations, and thus the fiber can be handled without altering the propagation properties. Hollow core fibers come in different designs, such as the simple tube waveguide (loss 0.95 dB/m) [23, 29], the anti-resonance waveguide (loss <0.0434 dB/cm) [44], the Bragg fiber (loss 0.9 dB/cm) [30], and the hollow core bandgap fiber (loss 1 dB/m) [41, 42, 45].

Alternatively the waveguides can be inspired by the work of the microwave community where metal waveguides are common, in the form of parallel plate [20, 21], tube [17, 18] or wire [22].

Chapter 3

Manufacturing of polymer fibers

One very important part of this project was the manufacturing of the THz fibers. This was done on a draw tower intended for manufacturing polymer optical fibers. The THz fibers are an intermediate step towards polymer optical fiber therefore the capability to manufacture THz fibers was already in place at the beginning of the project. Building upon the settings used when manufacturing polymer optical fibers, the settings and values presented in this chapter have been found through trial and error to result in high quality THz fibers. The full dynamics of the polymer draw and the complex issues of polymer behavior have not been fully explored in this project as these issues are outside the scope of the present thesis.

3.1 Presentation of the draw tower

The tower consists of two ovens, one conventional resistive oven and one infrared (IR) oven. The infrared oven is placed above the conventional oven. The idea of this configuration is that the infrared oven is intended as a pre heater and the conventional oven as the main draw oven. In the manufacturing of THz fibers the IR oven is not used. Above the oven the draw tower has a holder that can be extended into the oven, the preform is fixed to this holder. A picture of the draw tower is seen in Fig. 3.1

Below the oven there is a fiber puller, consisting of two soft plastic wheels that clamp on the fiber and pull it down. As the draw tower is intended for manufacturing polymer optical fibers it also has additional equipment consisting of a fiber diameter measuring unit, a capstan and a fiber pickup. These extra features are not used during the THz fiber drawing.

The tower has a holder centered above the ovens which can be lowered and raised. This holder is used to hold the preform. The preform is lowered into the oven and can be moved freely in the horizontal plane in order to

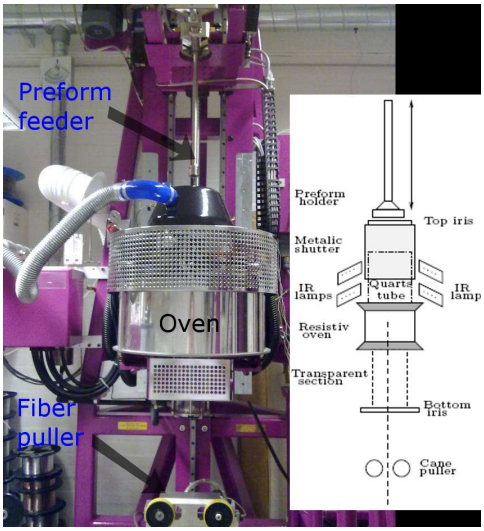

Figure 3.1: Picture of the draw tower. Inset shows a skematic of the draw tower

center it. During the draw the holder is lowered at a constant speed.

The tower functions are controlled by a control console next to the tower. This console also tracks and displays information from the tower such as temperature and position.

3.2 Preform preparation

The materials used in this project are poly(methyl-methacrylate) (PMMA) and Topas. The PMMA is acquired from an industrial provider and is bought in the form of 2 meter rods. One crucial detail regarding these rods is that they have to be manufactured by extrusion and not by casting. If cast PMMA is used it fills with bubbles during heating, most likely due to high concentration of free monomers. The extruded PMMA does not suffer from this problem. The Topas is acquired from *TOPAS advanced polymers GmbH* in the form of granulates. The granulates are cast into rods by Henrik K. Rasmussen at DTU Mekanik, Mechanical department. Both the PMMA and Topas are then processed at the mechanical workshop at DTU Fotonik. At the workshop the raw rods are machined into 100 mm long and 60 mm diameter cylinders before the computer numerical controlled (CNC) drilling machine drills the wanted hole pattern into the preform, an example of such a preform is seen in Fig. 3.2. The number of holes that can be drilled into the preform is limited by the drill bit size. The preferred size of drill bit for the workshop is 3 mm in diameter and the deepest they can drill using this bit is 80 mm. The workshop has also been able to make preforms using 2

mm drill bits to the same depth and 1.5 mm to only 50 mm depth. Using bit sizes smaller than 3 mm requires more work and attention. Drilling the hole pattern is one method that works well for polymers as polymers are machinable. However, even though the drill bits are much harder than the polymer, the drill bits have a surprisingly short life time. The polymer causes undetectable wear to the cutting edge of the drill bit causing the drill bit to excessively heat the polymer and ending in an catastrophic polymer melt, locking the bit inside the polymer. The only remedy is to replace the drill bits frequently. The drilling of the hole pattern is not the only way to achieve a hole pattern in a preform. At least two other methods exist. The first is stacking, where smaller polymer tubes are stacked together to make the final preform. This method can also be used to stack the final fiber: in particular when manufacturing teflon fibers it is necessary to stack the final fiber as teflon can not be processed in a draw tower. The second is to extrude either the preform or the fiber directly from granulate. This method allows for exotic patterns and holes that diverge from the circular [46]. However this method requires the costly manufacturing of the extrusion bit/mask. The draw tower has the capability of drawing preform of smaller diameter than the chosen 60 mm, however this has not been used in this project, because smaller preforms require drilling smaller holes to preserve the same structure.

Figure 3.2: Picture of a Topas preform. Inset shows a schematic with dimensions of the preform

3.3 THz fiber draw process

The THz fiber draw process consists of placing the preform in the oven and centering it, waiting for the preform to heat up and make a drop, place the drop in the fiber puller and draw the fiber. Placing the preform in the oven is done by lowering the holder with the preform down such that the bottom of the preform is approximately 10 mm above the oven. Positioning

the preform above the oven might seem contradictive, but it is an effort to ensure that the hot zone is not too large, Fig. 3.3(a). After the preform is centered in the oven it takes 1 1/4 - 1 3/4 hour before the drop is formed. The required time varies with temperature, material and fiber structure. The drop is formed when a region low on the preform becomes soft enough for the weight of the bottom of the preform to start falling from the preform as seen in Fig. 3.3(b). After the drop the THz fiber is drawn using the fiber puller and the transition section from preform to terahertz (THz) fiber, the neck down, stays in the hot zone, Fig. 3.3(c).

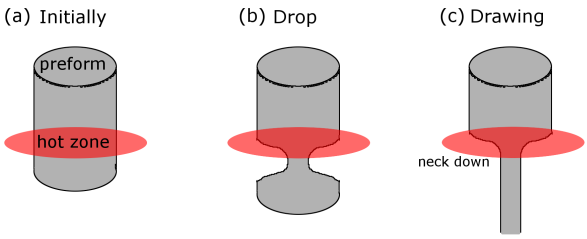

Figure 3.3: Drawing showing the transition from initial preform through drop to the THz fiber draw.

3.4 Manufacturing aspects

The temperature needed to make PMMA soft is around 105 °C [47] and the temperature needed to make Topas soft is around 78 °C [48]. The set draw temperature for PMMA is 300-350 °C and for Topas 250-300 °C. The temperature is set this high first of all because there is an offset between the set temperature and the actual temperature inside the oven. This offset is approximately 100 °C. Secondly the applied temperature has to be higher than the softening temperature since there needs to be a local hot zone, if the temperature is too low then the preform will be able to distribute the temperature through out the preform and there will not be enough local softening. One other reason for the high temperature is that during the draw there is a constant influx of material in to the hot zone and simultaneously a outflux of already hot material. This influx of cold material needs to be compensated for by using high temperature.

Ideally the transition zone should remain stationary. In this case the diameter of the THz fiber is given from simple conservation of mass. The mass going in to the transition zone must be the same as the mass coming out of the transition zone. The mass going in is given by the cross section of the preform multiplied by the speed of the preform, called feeding speed v_{feed}. The mass coming out is given by the cross section of the THz fiber

and the fiber draw speed v_{draw}:

$$r^2_{preform} v_{feed} = r^2_{fiber} v_{draw}$$

Unfortunately the relation does not always hold. In most cases the draw is instable, either the neck down is moving down or it is moving up.

When the drop has been processed and the draw is running, the hole size is monitored by taking samples from the draw. Typically the THz fibers are around 5-7 mm corresponding to a scaling down factor of 10. This scaling down factor is the most easily achievable and seems to be the product of a natural balance of the forces affecting the fiber draw. Both thinner and thicker fibers can be manufactured, the quality of these fibers is determined by how stable the draw is. Fibers of 1 mm and 10 mm diameter have been manufactured. This thickness is controlled using the draw speed. The typical draw speed is 150 mm/min and the typical preform feed speed is 1 mm/min.

The hole size inside the THz fiber respond to the draw temperature. The two extremes are hole collapse on one side when the temperature is too high and on the other extreme, at low temperatures, the fiber material being stretched to the point of fracture due to the expanding holes. Acting on experience the operator of the tower can respond to the fiber behavior by adjusting either the temperature or the draw speed always using small adjustments as the response of the fiber to the adjustments is slow.

3.5 Mechanical properties of THz polymer fibers

In order to understand the possibilities and limitations of the THz fibers in real life applications it is necessary to understand the mechanical properties of the THz fiber. Being made of polymer the THz fibers are soft and flexible. The stiffness of the material can be described using the Young's modulus (tensile modulus), the Young's modulus of PMMA is 3.1 GPa [47] and the Young's modulus of Topas is 2.2 GPa [48]. The low Young's modulus of the polymers indicates that they are soft, the Young's modulus values are approximately 25 times lower than the Young's modulus of silica (table 1.1 in [46]) and aproximatly 70-100 smaller than the Young's modulus of steel (table 3.1 in [49]). However the stress that the polymers can endure before breakage is described using the tensile strength: for Topas the tensile strength is 57 MPa[48] and the tensile strength of PMMA is between 48-76 MPa[47].

The strength of the polymers is only a factor of 10 lower than that of steel and is twice the tensile strength of silica. The polymer fibers are more flexible than silica and steel and they can also tolerate more stress than silica. As an example, consider a cantilever test of a 5 mm diameter and 10 cm long THz fiber, one end being fixed and the other end free to move as seen

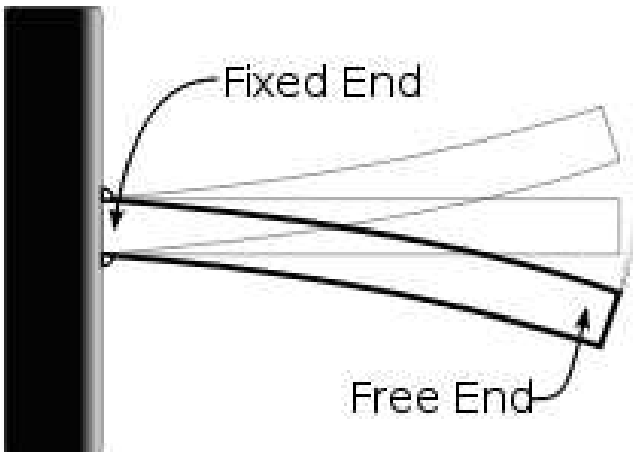

Figure 3.4: Cantilever test.

in Fig. 3.4. Assuming the applicability of the Euler-Bernouilli equation, if the fiber was made of silica, the fiber would break after applying 4 N of force down on the end of the fiber and the end of the fiber would deflect 0.9 mm before breaking. For steel the force needed to break the fiber is 74 N and the deflection is 4 mm. For PMMA the force needed is 7.4 N and the deflection is 26 mm and for Topas the same force is needed but the deflection is 37 mm. For it to be possible for a silica fiber to deflect as much as a 5 mm thick Topas THz fiber, the silica fiber would have to be approximately 100-150 µm in diameter. This is the same thickness as optical silica fibers, thereby the Topas THz fiber could be said to be as flexible as an optical fiber. However optical silica fibers are typically coated with polymer in order to make them more flexible. Larger deflections are possible if the polymers are heated up, but in this case the bend is permanent[1]. An example of Topas THz fibers bend into 90°bend is shown in Fig. 5.8 on page 38.

3.6 Cleaving of THz fibers

For THz fiber applications the fibers have to be terminated in such a way that the end facet of the THz fibers is relatively plane and smooth. When working with polymer optical fibers this is achieved by using the hot blade method, where the fiber is heated to soften it and then cut through using a sharp blade. THz fibers are too thick for this method to work, firstly the thickness makes it difficult to achieve a evenly distributed heating and secondly the razor blades usually used in the hot blade method are not strong enough to cut through even a soft THz fiber.

The quick way to achieve a cleave is by scribing the surface of the fiber and then breaking it along the cut. This is similar to the cantilever test

described earlier. If a cut is introduced at the point of highest stress, at the root of the cantilever, then the stress from bending the fiber will push a crack all the way through the fiber. The result is a almost plane cut with a rough surface.

If better quality surface is required then the end facet of the cleaved fiber can be processed using a milling machine. Lathe machining has also been attempted but the results from the milling machine are smoother. One disadvantage of the milling is that debris from the milling can fall into the holes of the THz fiber. The qualitative difference between the unmilled and the milled end facet can be seen in Fig. 3.5.

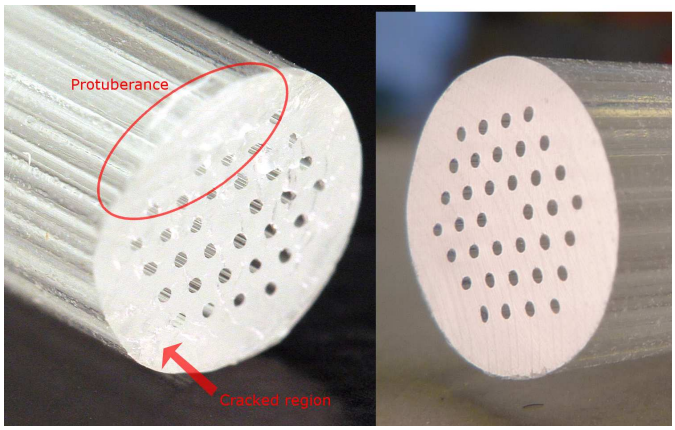

Figure 3.5: Picture of same Topas THz fiber. Left side is cleaved by scribing and breaking, as described in text. Right side has been milled after cleaving.

Chapter 4

THz characterization setup

The THz characterization of the polymer THz fibers was performed on an existing THz photoconductive antenna setup intended for terahertz time-domain spectroscopy (THz-TDS). The emitter and receiver of the THz setup were not altered during this project, only their position and the optical path between the two units was altered. In this chapter the THz system is presented and means for characterizing the polymer THz fibers are explained.

4.1 Photoconductive antenna THz system

A very popular way of generating coherent THz radiation is using the photoconductive antenna [50]. In this scheme the THz radiation is generated by acceleration and decelerations of electrons. The electrons act as a driving current $\mathbf{J}_{free}$ as known from Maxwell's equations. The electrons are generated by impinging an optical pulse on a semiconductor. The acceleration of the electrons is achieved by applying a bias over two closely spaced electrodes. The short life time of the free electrons, needed to get THz radiation, is achieved by having defects in the semi-conductor. Typically the semi-conductor is low-temperature grown GaAs. The impinging optical pulse is a 100 fs 800 nm pulse generated by a mode locked laser with a repetition rate of 80 MHz. The THz-TDS system in our lab is able to generate THz pulses with frequency components from less than 0.1 THz to above 3 THz.

Fig. 4.1(a) shows the basic design of the THz emitter. The optical pulse hits the semiconductor between the two biased electrodes and a THz pulse is generated. The polarization of the THz pulse is given by the arrangement of the electrodes. In Fig. 4.1(b) the basics of the THz detector is illustrated. In this case the bias over the electrodes is replaced by a locked-in current amplifier that detects the acceleration of the free electrons generated by the optical pulse. These two antennas form the basis of the THz-TDS and define the possibilities and limitations of the THz radiation range that has been

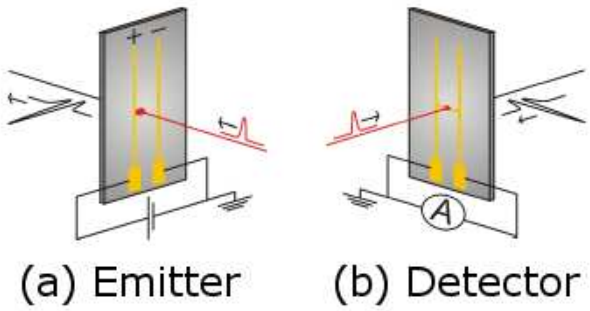

Figure 4.1: Basic principle of photoconductive antennas for generating and detecting THz radiation. The optical pulse is illustrated as a red line

investigated in this project.

Other ways of generating THz radiation exist. Based on nonlinear crystals it is possible to purely optically generate and detect THz radiation, applying optical rectification for generating THz radiation, and the Pockels effect for detecting the THz radiation [50].

4.2 THz Time domain characterization

A typical THz-TDS setup is shown in Fig. 4.2. The generated THz pulse is directed via gold coated mirrors through a sample to the receiver antenna.

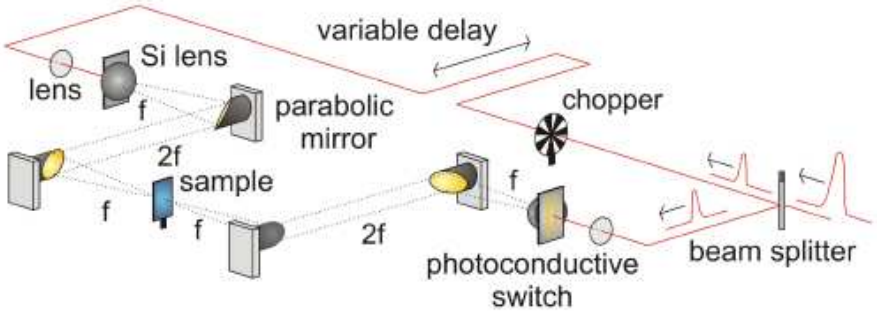

Figure 4.2: Basic working principle of THz-TDS.

The transmission through the THz setup is given by

$$E(\omega)_{det.} = E(\omega)_{emit} t_{12} t_{21} \exp(-i(-i\alpha(\omega)d/2 + \frac{\omega n(\omega)d}{c})) \qquad (4.1)$$

where t_{12} and t_{21} are the Fresnel transmission coefficients defining the transmission at the interfaces of the sample and d is the sample thickness. When making a reference transmission through dry air, the transmission coefficients are unity and the absorbtion coefficient is vanishing. To complete the spectroscopic measurement the transmission through a sample is normalized to a reference transmission without sample.

$$T = E(\omega)_{sample}/E(\omega)_{ref} \tag{4.2}$$

$$= \frac{E(\omega)_{emit} t_{12} t_{21} \exp(-\alpha(\omega)d/2) \exp(\frac{-i\omega n(\omega)d}{c})}{E(\omega)_{emit} \exp(\frac{-i\omega d}{c})} \tag{4.3}$$

$$= t_{12} t_{21} \exp(-\alpha(\omega)d/2) \exp(\frac{-i\omega[n(\omega)-1]d}{c}) \tag{4.4}$$

It is possible to find the absorbtion $\alpha(\omega)$ by first investigating the phase of T to find the refractive index $n(\omega)$, and then use the refractive index to calculate the Fresnel coefficients $t_{12}t_{21}$.

4.3 THz-TDS characterization of polymer fibers

The three THz-TDS setups used in this project are illustrated in Fig. 4.3. Fig. 4.3(a) shows the standard setup, it is similar to a typical THz-TDS where the sample has been replaced with a fiber, with or without the lenses. The strength of this setup is that it is easy to align and it has a good signal to noise ratio. It is always used for the initial investigation of the fiber, particularly in terms of the transmission bandwidth. The optional lenses are made of Topas and can be independently positioned such that the optimal coupling can be reached. However the lenses introduce extra material and this is particularly important at high frequencies where the material loss is high, therefore the lenses are not included when investigating hollow core fibers.

The setup in Fig. 4.3(b) is needed when investigating 90° bend fibers. This setup is difficult to work with because it introduces extra freedom of movement that can complicate the setup alignment. When making cut-back measurements the length of the fiber under investigation is not constant. For cut-back measurement the setup in Fig. 4.3(a) is not suitable because the radiation coupled in and out of the fiber depends on the distance between the fiber and the antenna, and in order to get the correct propagation loss the coupling must be kept constant. To overcome this problem the reflection setup shown in Fig. 4.3(c) was constructed, where the input and output coupling are the same and are kept constant. The reflection at the back end of the fiber is ensured by a metal foil applied to the end of the fiber. The waveguide absorption and effective refractive index can be extracted by

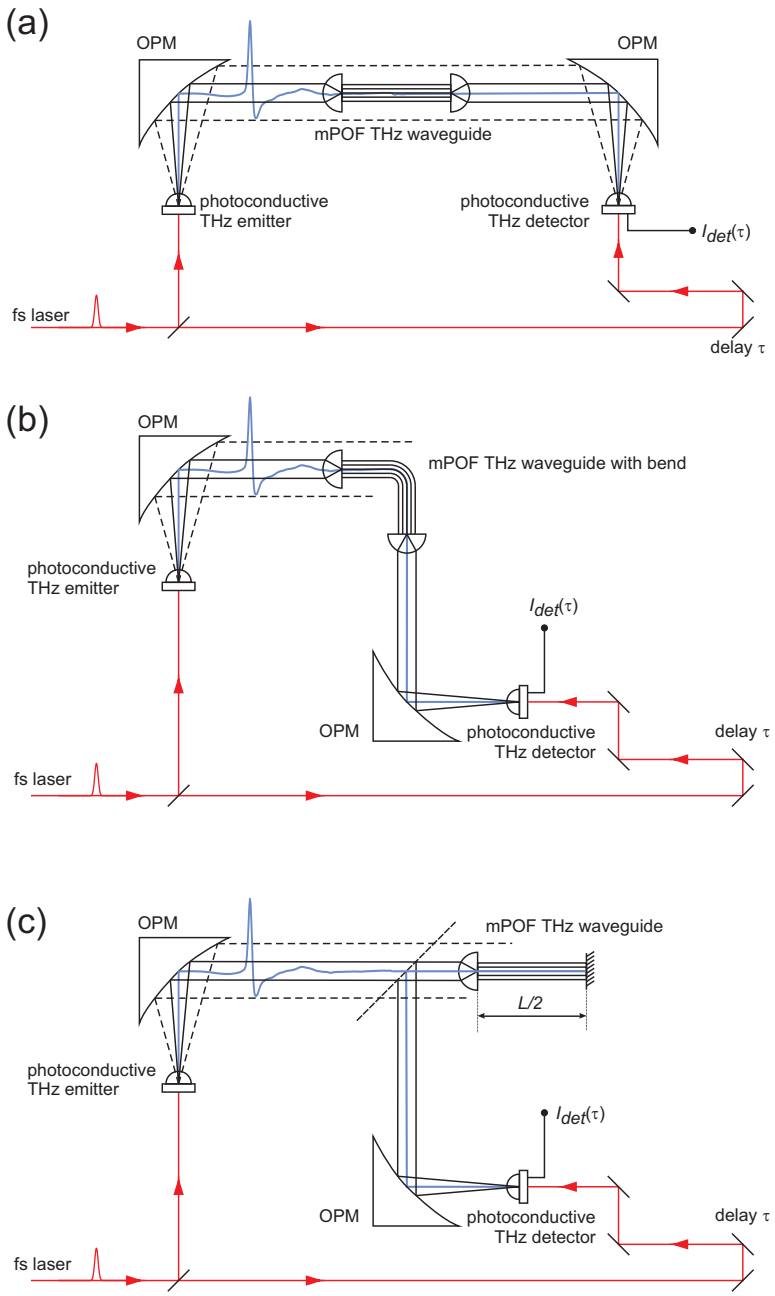

Figure 4.3: Three different configurations used in this project to characterize THz polymer fibers. OPM is off-axis parabolic mirror.

comparing the transmission through two different fiber lengths, $L1$ and $L2$:

$$T = E(\omega)_{L1}/E(\omega)_{L2} \tag{4.5}$$

$$= \frac{E(\omega)_{emit}c_{in/out}\exp(-\alpha_{eff}(\omega)L1/2)\exp(\frac{-i\omega n_{eff}(\omega)L1}{c})}{E(\omega)_{emit}c_{in/out}\exp(-\alpha_{eff}(\omega)L2/2)\exp(\frac{-i\omega L2}{c})} \tag{4.6}$$

$$= \exp(-\alpha_{eff}(\omega)(L1-L2)/2)\exp(\frac{-i\omega n_{eff}(L1-L2)}{c}) \tag{4.7}$$

Where the coupling $c_{in/out}$ vanishes together with the emitted field.

Chapter 5

Solid core THz PCFs

In this chapter the solid core structured polymer fibers for guiding of THz radiation is presented and analyzed. The fibers are made of Topas and are expected to demonstrate low loss and low material dispersion. The fibers are analyzed using a THz time domain spectroscopy setup. A dispersion analysis of the transmitted THz pulses shows that the fibers display regions of normal and anomalous dispersion and also shows that the fiber can have losses lower than the bulk material loss. A near-field characterization of the modal structure demonstrates single-mode propagation over a wide frequency range and an onset of higher-order mode propagation at high frequencies. Finally the guided propagation is proven to be tolerant towards sharp bends of the fiber due to the strong confinement of the field in the solid core of the fibers.

5.1 Description of the fibers

Two fiber designs have been drawn: a Large Mode Area (LMA) fiber and a Small Mode Area (SMA) fiber. An image of the fibers is shown in Fig. 5.1. The LMA fiber has a pitch of 560 μm and a hole diameter of 250 μm giving a hole diameter to pitch ratio of approx. 0.45. The SMA fiber has a pitch of 350 μm and a hole diameter of 280 μm giving a ratio of approx. 0.8.

The hole diameter to pitch ratio gives an indication of the mode characteristics of the fiber. A low hole to pitch ratio gives a fiber that is single mode and a large ratio gives a fiber that is multi mode. This relation is well known from optical fibers as reported by Mortensen *et al.* [51]. However at short lengths many modes may exist.

A contour plot of the spatial profiles of the electric field of the lowest modes in the LMA and the SMA fibers at a frequency of 1 THz are shown in Fig. 5.2, calculated using COMSOL. Together with the mode profile the position of the air holes is shown. The effective areas of the SMA mode and the LMA mode are 0.11 mm^2 and 1.86 mm^2, respectively, at 1 THz.

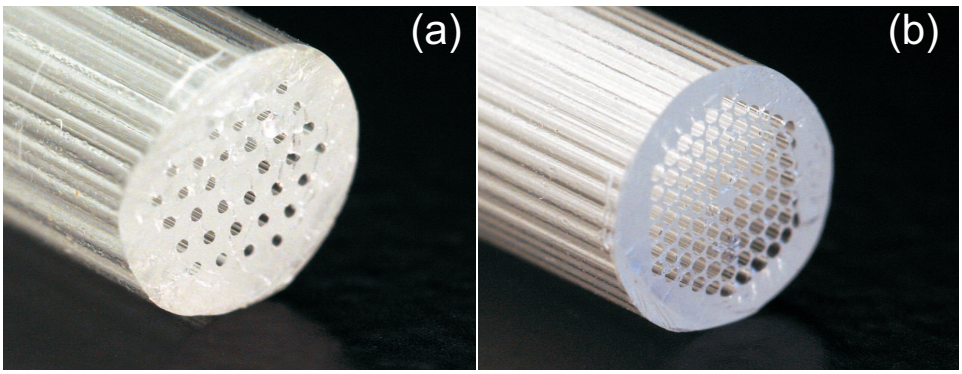

Figure 5.1: (a) Image of the large mode area (LMA) fiber. The outer diameter of the fiber is 6 mm. The diameter of the holes is 250 μm and the pitch is 560 μm. (b) Image of the small mode area (SMA) fiber with an outer diameter of 5 mm, diameter of the holes of 280 μm and pitch 350 μm.

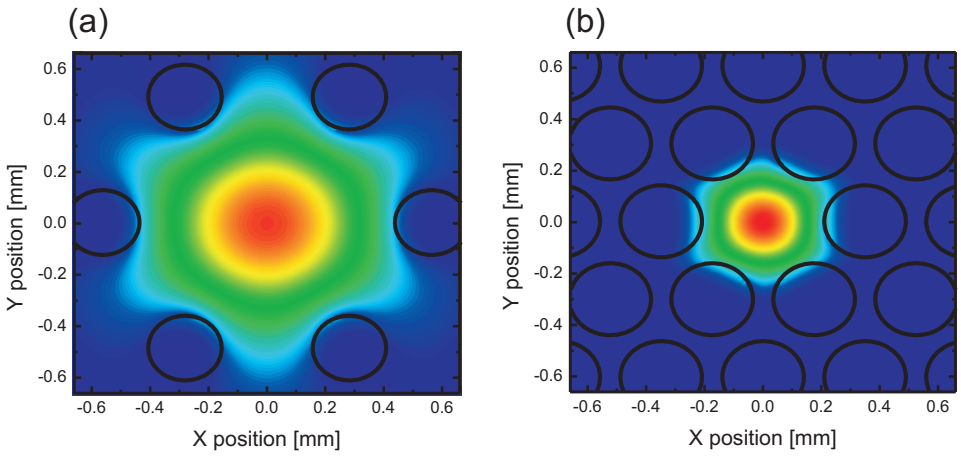

Figure 5.2: Calculated mode profiles of the (a) LMA fiber and (b) SMA fiber at 1 THz.

5.2 THz near-field and far-field measurements

The experimental investigation of guided propagation through the SMA and LMA THz fibres was carried out using two variations of terahertz time-domain spectroscopy (THz-TDS). Near-field measurements were performed by Dr. Plankens group at Delft University of Technology in the Netherlands. The modal structure of the THz field propagating through the fibers was measured directly at the end facet of the fiber using a near-field probe. The high spatial resolution required for the direct modal characterization was obtained by coupling of a freely propagating single-cycle, broadband THz pulse onto one end facet of a piece of the fiber, and positioning the other facet of the fiber directly on a gallium phosphide electro-optic field sensor. This sensor measures the temporal profile of the transmitted THz field by ultrafast free-space electro-optic sampling using a tightly focused beam of femtosecond laser pulses split off from the beam of pulses generating the THz pulses [52]. The spatial resolution was 10 μm, determined by the focal spot size of the probe beam. This corresponds to a deep sub-wavelength resolution of $\lambda/300$ at 100 GHz, and $\lambda/30$ at 1 THz.

5.3 Cutback measurement

For the measurements of fiber dispersion and loss a standard THz-TDS system was used. The THz-TDS setup is modified to allow either transmission measurements of straight and bent sections of fiber or reflection measurements at normal incidence for the cut-back loss measurements in order to assure identical coupling in and out of the different fiber lengths. In the reflection configuration the terahertz (THz) signal is reflected at the back end facet of the fiber by a metallic reflector in close contact with the fiber facet, and hence it traverses the fiber length two times, the setup is seen in Fig. 4.3.

The collimated THz beam is wider than the diameter of the fiber cores of approximately 0.5 - 1 mm. Therefore Topas hyperhemispherical lenses are manufactured for better coupling between the collimated free-space THz beam and the guided mode in the fibers. Compared to a silicon hyperhemispherical lens, the Topas lens has a much lower refractive index. This results in lower reflection losses at the dielectric interfaces while keeping a good overlap between the free-space mode and the guided mode.

In Fig. 5.3 the properties of the pulse propagation through the two fibers is shown. Panels (a) and (b) show the spectrograms. The spectrogram is calculated by making a Fourier transform of the convolution of the transmitted data and a 3 ps Gaussian pulse. of THz pulses after propagation through 26 mm SMA fiber and through 29 mm LMA fiber, respectively. Overlaid on the spectrograms are the time traces of the electric field of the THz pulses.

At early times (not shown here) we observe a small signal due to a slight leakage of the THz field around the fiber. The position of the main signals relative to this leakage signal was used to verify that the observed signals are indeed guided modes. The ringing after the main pulse, particularly clear on the LMA trace, is caused by rotational transitions in the water vapor in the atmosphere excited by the broadband THz pulse.

The strong dispersion of the SMA fiber results in a temporal stretching of the THz pulse to several tens of picoseconds after propagation over the relatively short distance of 26 mm in the fiber. In contrast, the LMA fiber displays a rather small dispersion, as expected from the above discussion of the mode profiles.

For direct comparison with numerical predictions the calculated dispersion parameter $D = (1/c)(\nu\partial^2 n_{\text{eff}}/\partial\nu^2 + 2\partial n/\partial\nu)$ of the fundamental mode in each fiber is shown in Panels (c) and (d) of Fig. 5.3.

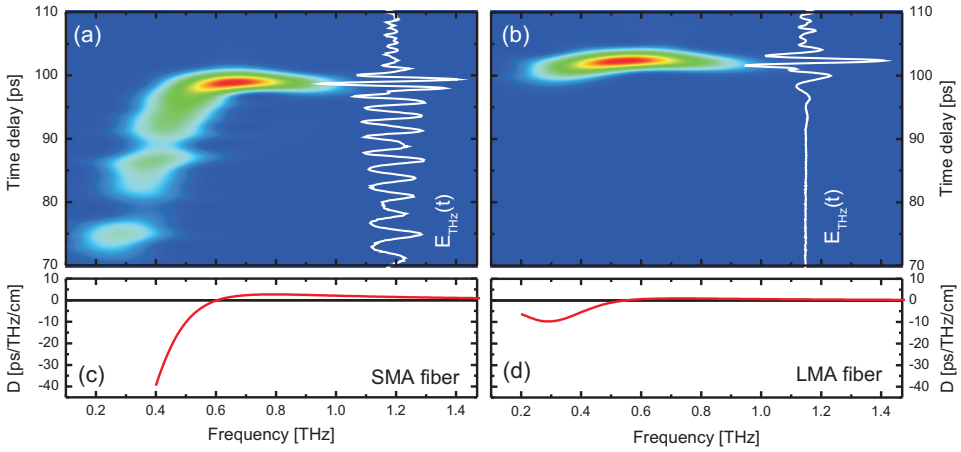

Figure 5.3: Spectrogram and temporal profile of the THz pulse after propagation through 26 mm SMA fiber (left) and 29 mm LMA fiber (right). The graphs under the spectrograms show the dispersion parameter D for each fiber.

In order to measure the loss of the fiber a cutback experiment is performed, where transmission measurements in a double-pass reflection geometry are carried out on the fibers ranging from 2.5 mm to 53 mm, corresponding to propagation lengths from 5 to 106 mm, as illustrated in the inset of Fig. (5.4). Using this geometry assures that the free-space beam path of the THz spectrometer as well as the coupling in and out of the fiber is kept constant during the measurements on different lengths of the fiber.

The black squares in Fig. 5.4 shows the power attenuation $10\log(\sum_{t=0}^{t=\infty} E(t)^2)$ of the THz signal as function of the LMA fiber length L. The summation is made over the transmitted amplitude of the pulse in time. A linear fit to the experimental data shows a loss of $\alpha_{dB} =$

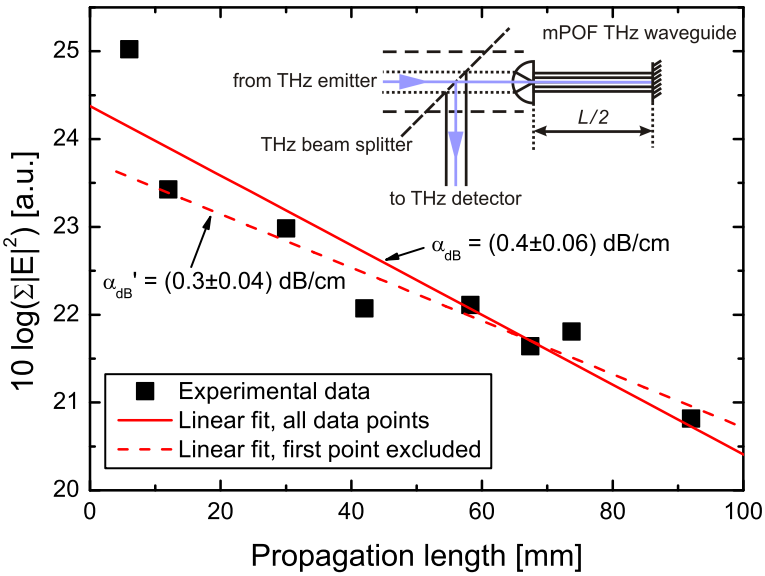

Figure 5.4: Determination of the frequency-averaged loss of the LMA fiber. The inset shows the experimental configuration for the cutback measurement. The full line shows a linear fit including all data point, the dashed line shows a fit excluding the first data point.

(0.4 ± 0.06) dB/cm, or an average absorption coefficient $\alpha = 0.089$ cm^{-1}. The experimental measurements indicate a high initial loss rate, possibly due to radiative loss at the beginning of the fiber due to imperfect mode matching between the guided mode and the free-space mode, so called "over-launched condition" [46]. If the first data point is removed from the linear fit then the loss reduces to $\alpha'_{dB} = (0.3 \pm 0.04)$ dB/cm, or an average absorption coefficient $\alpha' = 0.067$ cm^{-1}, averaged over the bandwidth of the pulse. These values are lower than our measurement of the average material loss of Topas in the 0.1-1 THz region ($\alpha_{bulk} \approx 0.15$ cm^{-1}) and indicating that in spite of the tight confinement of the propagating mode to the solid core of the fiber, a significant portion of the field propagates in the lossless air regions of the fiber. In Fig. 5.5 the frequency dependent loss is shown. This loss spectrum is obtained by analyzing the full spectrum of the transmitted THz radiation through the LMA fiber at different lengths. It shows a frequency range between 0.4 THz and 0.6 THz where the propagation loss is significantly lower than the bulk loss of Topas. The lowest loss at around 0.5 THz is less than 0.1 dB/cm. At lower frequencies the loss rises, this increase in loss as the frequency drops is due to increased confinement loss. At higher frequencies the loss rises due to larger scattering sensitivity[53].

The effective index of the fiber is always difficult to extract, mostly due to the low signal to noise level, but also because the fibers effectively have

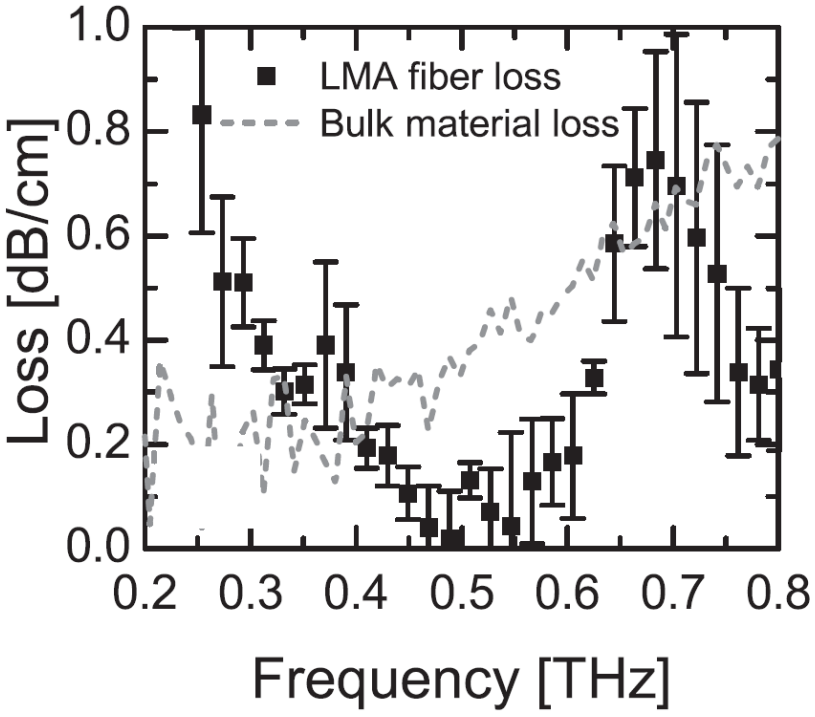

Figure 5.5: Determination of the frequency dependant loss of the LMA fiber. The dashed line shows the bulk loss of Topas, while the squares with error bars show the measured frequency dependant loss.

a low frequency cut-off making it difficult to keep track of the phase in the FFT of the time delay signal. However an attempt is made at extracting the effective refractive index of the LMA fiber by selecting the three best signals. They are selected because they produce relatively smooth results near the expected value. The resulting effective refractive index is shown in Fig. 5.6 together with the numerically calculated effective index. The difference between the experimentally measured effective index and the numerically calculated effective refractive index is large and hard to account for. One explanation could be that there is an offset in the measured index, possibly caused by bad data. The other explanation is more interesting: if this result is correct then it opens up the possibility that the material changes refractive index when drawn from bulk to fiber. If this is the case then it will have large implications on the whole fiber design process. Apart from making better measurements on the THz fibers, one way of investigating this is to make bulk measurements on a stretched plate of Topas, before and after stretching.

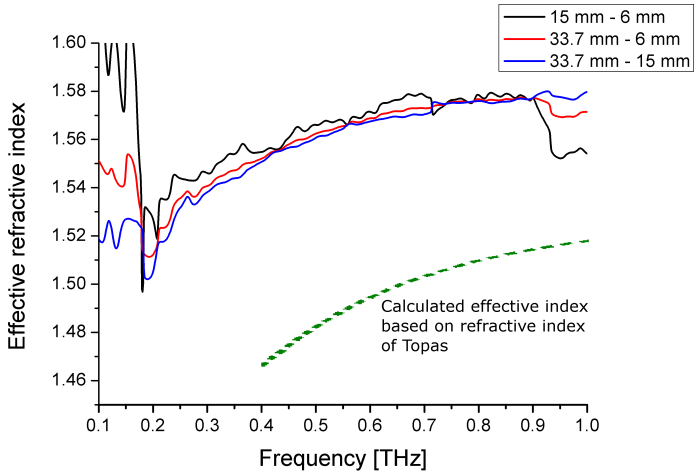

Figure 5.6: Measured effective refractive index based on three selected fiber lengths. The lengths in the legend refers to the length of the fibers used and the combination of fibers used to make the plot. The dashed line shows the expected numerically calculated effective refractive index.

5.4 Near-field measurements

The modal structure of the propagating mode was measured in the near field of the end facet of short fiber pieces. Panels (a) and (b) of Fig. 5.7 show the electric field distribution in the central region of the LMA fiber at 0.2 THz

and at 1.0 THz, and Panels (c) and (d) the corresponding field distribution in the SMA fiber.

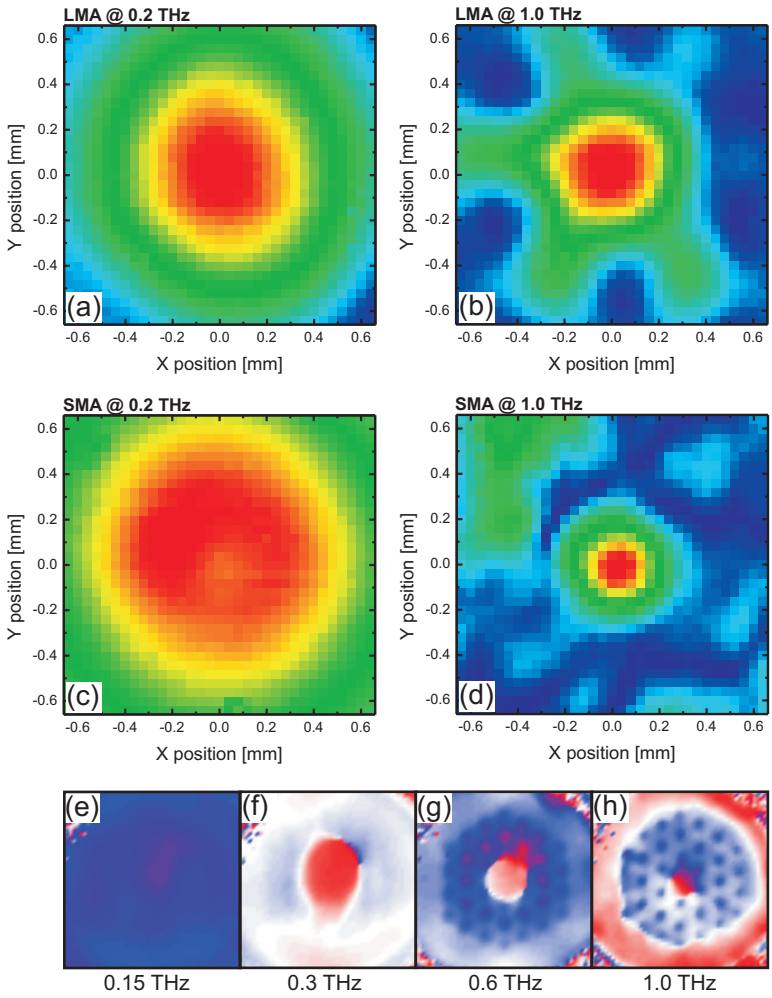

Figure 5.7: Experimentally determined modal structure of the propagating mode through the LMA fiber at (a) 0.2 THz and (b) 1.0 THz, and through the SMA fiber at (c) 0.2 THz and (d) 1.0 THz. The phase of the frequencies 0.15, 0.3, 0.6, and 1.0 THz are shown in the panels (e)-(h).

At 0.2 THz the field is better confined in the LMA fiber than in the SMA fiber, whereas at 1.0 THz the field is significantly more concentrated in the SMA fiber than in the LMA fiber, as expected from the modal calculation in Fig. (5.2). The larger mode area at 0.2 THz in the SMA fiber is a experimental observation similar to the guided propagation in a microporous fiber, as described numerically by Hassani *et al.* [43] and Atakaramians *et al.* [25]. At 0.2 THz the wavelength of the propagating mode is slightly larger than 3 mm, and with a hole pitch of only 350 μm the fiber cross section is very

similar to the microporous fiber cross section [25, 43]. This similarity breaks down in the LMA fiber with larger pitch and larger polymer fraction, and also at higher frequencies. In these situations the solid core of the photonic crystal structure acts as the guiding element, as evident from Fig. 5.7.

The stray light observed in the image of the SMA mode at 1 THz is most likely due to imperfect cleaving of the fiber. The large air filling fraction leaves the fiber facets rather sensitive to the cleaving method, and small fragments of polymer easily clog some of the air holes after cleaving.

Panels (e)-(h) in Fig. (5.7) show the measured distribution of the phase of the THz signal propagated through the LMA fiber at frequencies ranging from 0.15 to 1.0 THz, as indicated in the figure. At the lowest frequency a constant phase is observed across the whole fiber cross section, indicating that the fiber as a whole is responsible for the guiding. This can be interpret as a manifestation of propagation in an effectively microporous environment. At higher frequencies the phase of the field in the core region of the fiber is opposite of the phase of the signal in the cladding region of the fiber. This is a direct consequence of guiding in the fundamnetal mode in the solid core of the fiber. Interestingly, at the highest frequencies the onset of higher-order mode propagation in the solid core can be detected, seen as a phase shift across the core region. The insight into the guiding properties of the fibers offered by the amplitude and phase resolved near-field THz imaging is unique, and the data in Fig. 5.7 are unrivaled by current technology for characterization of similar effects in the near-IR.

5.5 Propagation through 90 degrees bends

The tight confinement of the propagating mode to the solid core of the fiber allows us to shape the fiber into sharp bends while still guiding the THz radiation. At room temperature the fiber is too rigid for a big bend, so in order to make a 90° bend the fiber is heat locally to above the glass transition temperature and then bend into shape. Using this approach we are able to make bends of almost any shape. A few examples of 90° bends are shown in Fig. 5.8

Although the measurement on the bent fiber is made difficult due to the lack of flexibility of the THz-TDS setup, a transmission is recorded through a 10 cm LMA type fiber bent with a 6.5 cm bend radius. The time trace of the transmission is shown in the inset of Fig. 5.9 while the focus of Fig. 5.9 is the spectrogram showing that the bandwidth of the transmission is limited to frequencies below 0.5 THz and the transmission is split up into two main groups. The limited bandwidth is explained by the propagation loss of the fiber as shown in Fig. 5.5

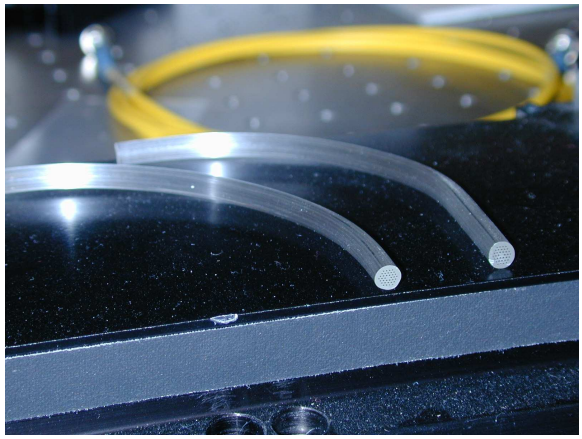

Figure 5.8: Images of two bent Topas fibres.

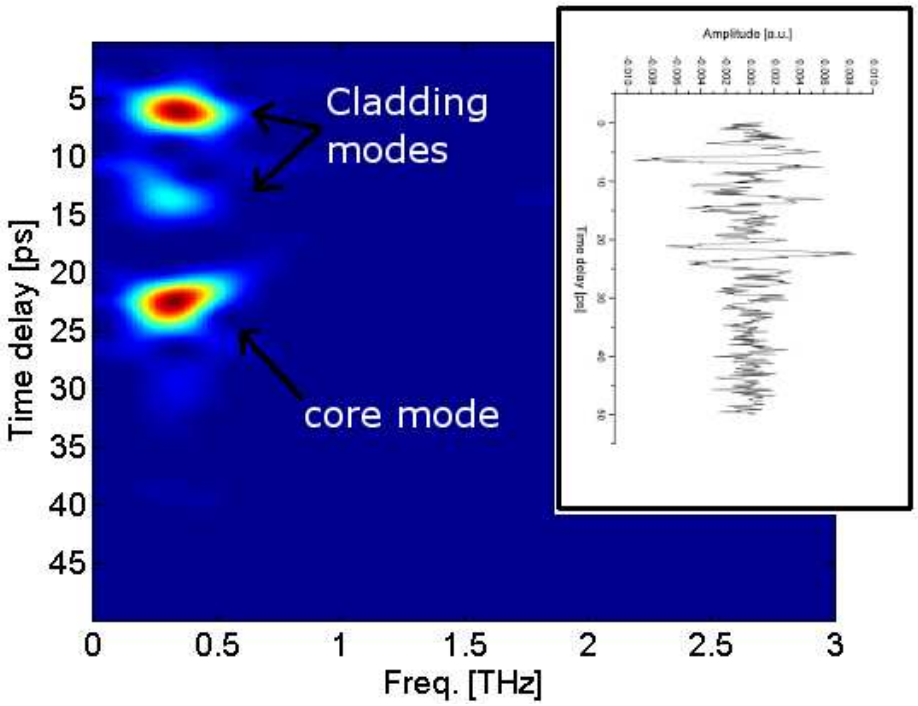

Figure 5.9: Spectrogram of transmission through 90° bend. Inset shows time trace.

5.6 Introducing a loss layer to strip cladding modes

One of the difficulties in doing cutback loss measurements on the SMA fiber was the high probability of exciting a cladding mode. The cladding modes have low loss and beat with the core mode, making it difficult to distinguish between the core mode and the cladding mode in the frequency domain. One way of stripping cladding modes from the transmission spectrum is to introduce an absorbing layer that overlaps well with the cladding modes in space while not overlapping with the core mode. This can be achieved by introducing a high loss polymer into the outermost holes of the cladding. The first difficulty is to effectively introduce this new material selectively into the holes. The solution is to use a polymer with a softening temperature well below the transition temperature of Topas, block the holes that are to be open, and fill this high loss polymer into the wanted holes. It is possible to selectively fill the holes because the fiber is thick enough that no special tools are needed. An image of the test fiber is shown in Fig. 5.10, it has extra big holes surrounding the cladding.

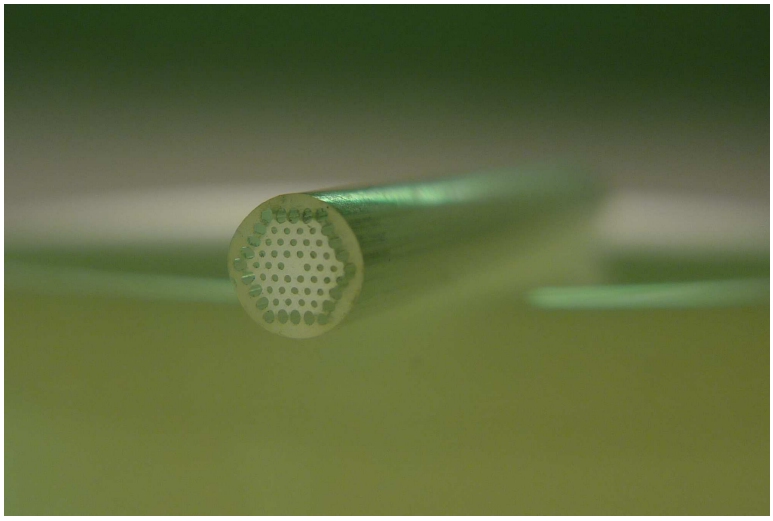

Figure 5.10: Image of THz fiber with extra holes for introducing absorbing media.

The fiber was investigated using THz-TDS before and after introducing the absorbing material, the time-traces are shown in Fig. 5.11. Compared to before introducing the absorbtion layer, the front end of the transmitted pulse has been attenuated. The front end of the pulse contains the modes which reach furthest into the cladding, making them more susceptible to the absorbing layer. This seems to indicate that this is a viable way to strip

cladding modes. More work is needed to ensure that the introduced absorption layer does not influence the guiding of the fundamental core mode.
Other ways of stripping cladding modes include scratching the surface along the length of the fiber to introduce scattering loss to the cladding modes. This technique is known from microstructured polymer optical fiber (mPOF)[46].

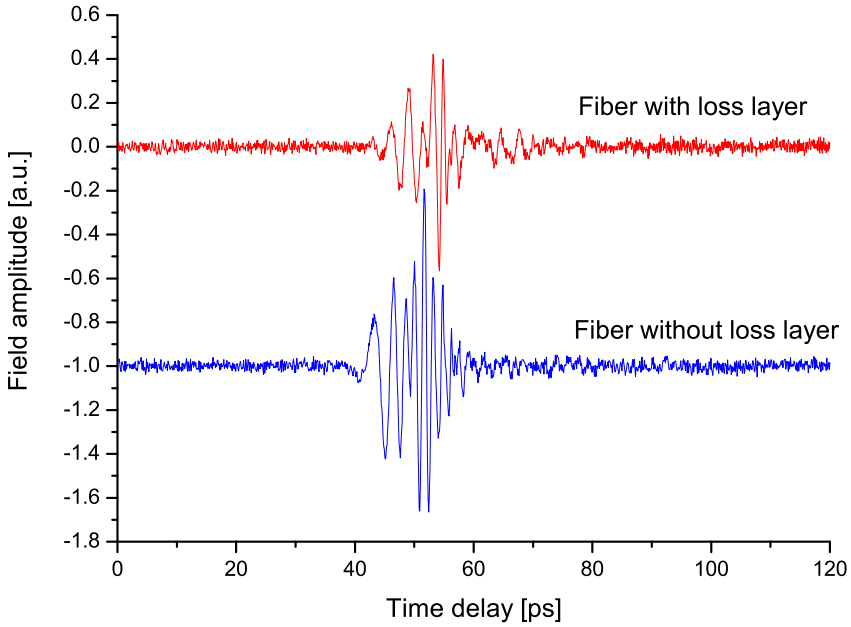

Figure 5.11: Time traces of fiber without loss layer and fiber with losslayer.

Chapter 6

Hollow core THz fibers

Hollow core fibers are interesting as THz waveguides as they hold the potential of lowest waveguide loss. In order to realize low loss the hollow core fiber guides the THz radiation in an air core surrounded by a structured cladding that prohibits the radiation from coupling out of the core. The way to achieve this inhibited coupling is by designing the cladding in such a way that it does not support any modes with an effective refractive index around the refractive index of the core($n_{air} = 1$), in as wide a frequency range as possible. This type of fiber is a novelty, and has been intensely studied in the optical range over the last decade since the introduction of the first silica hollow core photonic bandgap (PBG) fiber in 1999 by Cregan *et al.*[45]. Hollow core fibers also include the Bragg fiber and the Kagome fiber, where the Bragg fiber works essentially in the same way as a PBG fiber. The main difference being that Bragg fibers usually consist of concentric rings of alternating low and high index materials. The Kagome fibers work in a different way; the cladding does not provide a bandgap but rather there are frequency ranges where the cladding has very few, weakly coupling modes.

6.1 Topas THz hollow core fiber

Although the fiber design offering lowest loss is the hollow core design, there will always be some overlap between the mode and the material, therefore the material used should also have low loss. As Topas has low material loss, hollow core fibers made of Topas should have the lowest total propagation loss. A Topas hollow core fiber made in this project is seen in Fig. 6.1. It is 6 mm thick and has a triangularly structured cladding consisting of 5 rings around the core. The core is made by omitting 7 cells of the cladding, the core is 1.7 mm in diameter and is circular.

To compensate for the mismatch between a circular core and the more natural hexagonal structure obtained when omitting 7 cells, six holes adja-

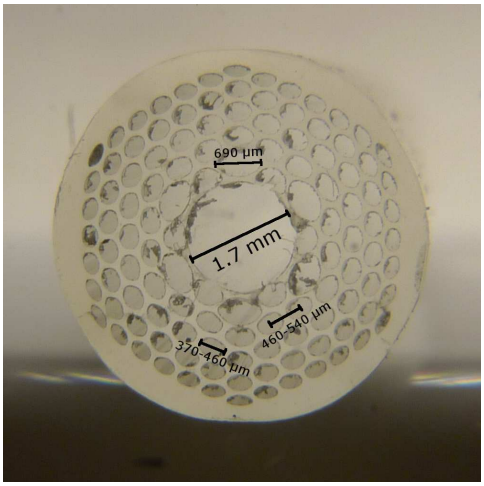

Figure 6.1: Image of the Topas hollow core fiber. The hole and pitch chirp are visible as a reduction in both hole size and pitch in the outwards direction from the core.

cent to the core have deliberately been made slightly larger than the rest. The preform was fabricated by drilling 3 mm holes in the cladding with a pitch of 4 mm. The 6 enlarged holes around the core are drilled as 4 mm holes and the core is made by drilling a 10 mm hole. After drawing the preform was scaled down by a factor of 10. As the initial hole diameter to pitch ratio of the preform is not high enough for bandgaps to appear, the manufacturing has been made using low temperature in order for the holes to expand. Unfortunately the central core expanded more than the rest and is pushing the rest of the structure outwards. This leads to an unwanted chirp in the structure and also causes the holes to become elliptical. The ellipticity of the holes is around 0.75. The hole sizes in the fiber vary between 370 µm and 460 µm in diameter and the cladding pitch is between 460 µm and 540 µm giving a hole to pitch ratio of around 0.8-0.85. The hole sizes and cladding pitch are chirped in the same direction. Ideally the hole to pitch ratio should have been higher than 0.95 and the cladding should have been more homogenous. Had this been the case then according to Pottage *et al.*[54] this structure would have led to a full bandgap at around 1 THz assuming a pitch of 500 µm. Although this structure can not provide a full bandgap, it can still provide frequency ranges where the cladding mode density is low. In these frequency ranges a core mode could exist and this core mode would then be guided by inhibited coupling in a similar way as the Kagome guiding. Again according to Pottage *et al.*[54], using the hole to pitch ratio of 0.8 and the same pitch the fiber will support a range of low mode density at around 0.7 THz and then a weak second order bandgap at around 0.9 THz and again a range of low mode density at around 1.2 THz

and 1.4 THz. Although the calculations in the Pottage *et al.*[54] paper are performed on a structure with a refractive index of 1.5, this is close enough to the refractive index of Topas of 1.528, that the results can be compared. In order to investigate the possibility of some core guidance being present in the fiber a THz transmission was attempted. The results of that transmission are shown in Fig. 6.2. A signal is transmitted through the fiber and the front of that signal is only delayed by 8 ps. Although the refractive index of the core mode is around 1, there can still be a delay in the transmission due to the group velocity. The group velocity is given as:

$$v_g = \frac{c}{n + \omega \frac{\partial n}{\partial \omega}}$$

The group velocity is influenced by dispersion($\frac{\partial n}{\partial \omega}$). Since the transmission consists of distinct transmission windows and each window edge introduces large dispersion, a small delay is to be expected.

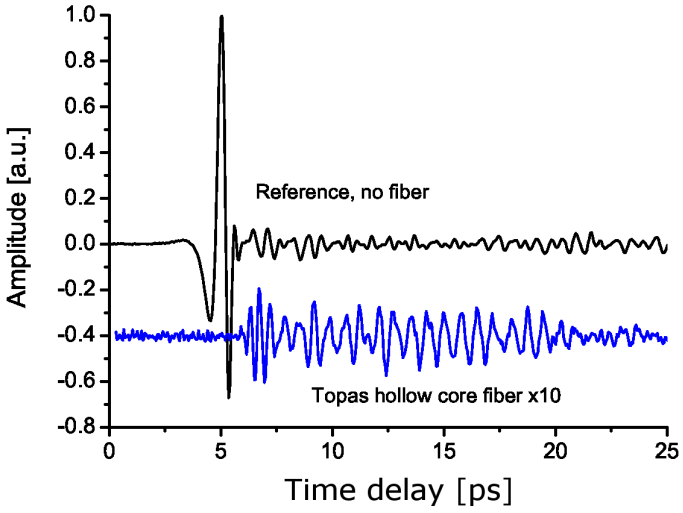

Figure 6.2: Time trace THz transmission through 44 mm Topas hollow core fiber together with a reference measurement without any fiber.

In Fig. 6.3 the frequency distribution of the measurement shows very good transmission at some frequency ranges while other frequencies are totally absent. The transmission fits well with the expected transmission windows. Both measurements are made without purging the setup with nitrogen, therefore there are many distinct absorption dips caused by water vapor. These dips manifest themselves in both the reference measurement as well as the fiber measurement. Apart from the vapor dips there are

additional dips, especially in the frequency range from 0.5 THz to 1 THz. These dips are most probably caused by either coupling from the core mode to cladding modes that are then attenuated, or beating between core mode and cladding modes. The dips can also be caused by an combination of both.

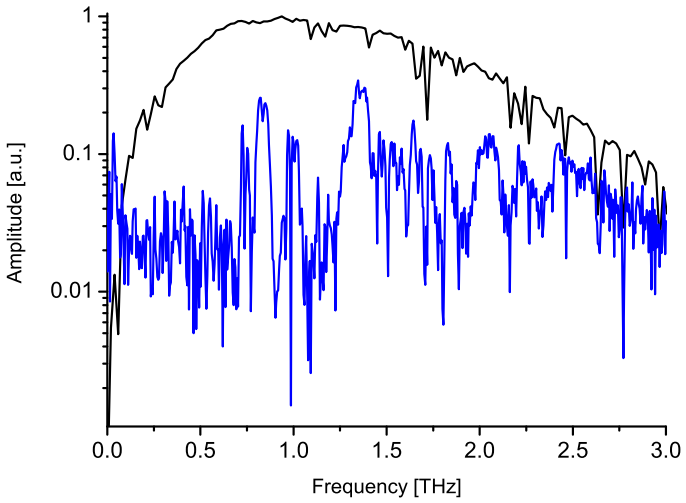

Figure 6.3: Frequency distribution of the transmission through Topas hollow core fiber together with the freqeuncy distribution of the reference measured with no fiber.

In order to distinguish core modes from cladding modes a spectrogram of the transmission data is calculated. The result is seen in Fig. 6.4. The spectrogram shows two groups of peaks, the high frequency group is the fastest through the fiber and consists of one main peak at around 1.4 THz and a tail stretching to 2.5 THz. This group is most likely core guiding as the group refractive index of this fast group is close to 1. The low frequency group are assumed to consist of cladding modes or surface modes glazing the inside of the core of the fiber. The cladding modes seem to be separated from the core modes both in frequency and in time meaning that the cladding modes must have been excited at the input of the fiber and transmitted through the fiber without interacting with the core mode. In any case these extra modes will cause beating in the transmission and are the cause of some of the dips in the frequency distribution seen in Fig. 6.3.

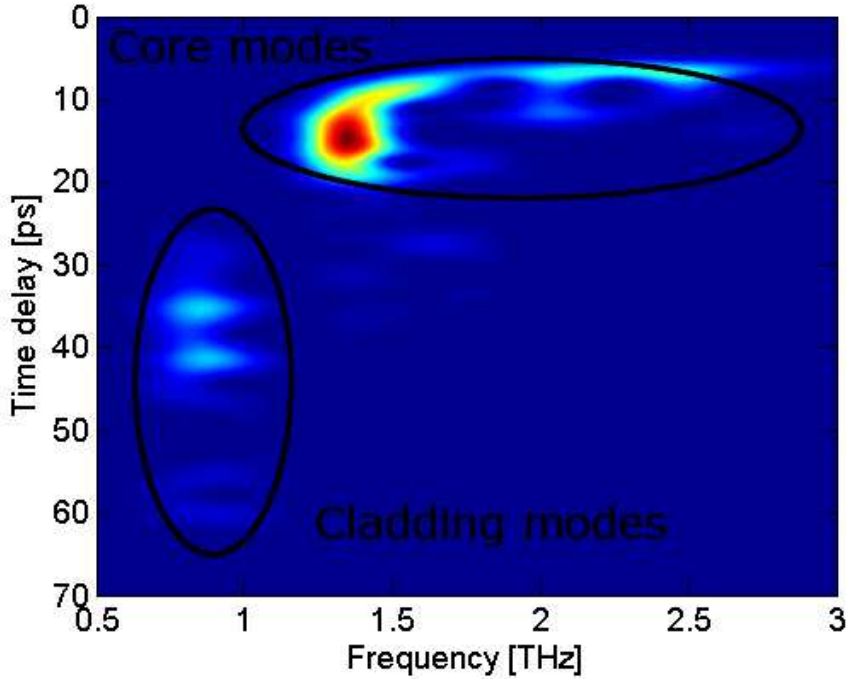

Figure 6.4: Time trace THz transmission through 44 mm Topas hollow core fiber together with the spectrogram showing the relation between the frequency and the time delay.

6.1.1 Near-field measurements

The Topas hollow core fiber was sent to Freiburg for near-field measurements by Prof. Walther's group at the University of Freiburg. The setup is seen in Fig. 6.5 more details on this setup and the near-field measuring technic can be found in the paper by Bitzer *et al.*[55].

From these near-field measurements we can see that there are indeed core modes supported by the fiber, see Fig. 6.6. It is interesting that the high frequency mode seen in Fig. 6.6(e) seems to be of a higher order than the low frequency modes. This corresponds well with our measurements showing a temporally broad pulse at around 1.4 THz. It is surprising that the low frequency modes, shown in Fig. 6.6(a),(b) and (c), are this well localized to the core.

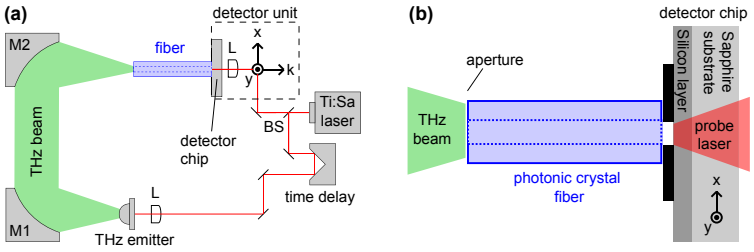

Figure 6.5: The near-field measurement setup at the University of Freiburg. The x-axis on the top graph is frequency in THz.

Due to the ability to accurately move the detector to ensure constant coupling while measuring on fibers of increasing lengths. The near-field setup at the University of Freiburg was also able to make a loss measurement. The loss figures for 0.64 THz and 1.5 THz are found to be 1.5 dB/cm and 0.7 dB/cm, however these values are based on only 4 fiber lengths and therefor more measurements are required before saying any thing definitive about the loss. It is however interesting that the low frequency loss is higher than the high frequency loss, corresponding well to the assumption that the low frequency modes have a fraction of their field propagating in material.

6.2 PMMA THz hollow core fiber

In the paper by Pottage *et al.*[54] where the authors perform numerical calculations on hollow core PBG fibers made of high index materials they find that a new robust bandgap opens up when increasing the refractive index. This new type of bandgap is reported to require a lower hole to pitch ratio. In the case of PMMA the hole to pitch ratio could be as low as 0.72, while the optimal hole to pitch ratio is 0.88. At this hole to pitch ratio the bandgap width should be approx. 8% at a normalized frequency

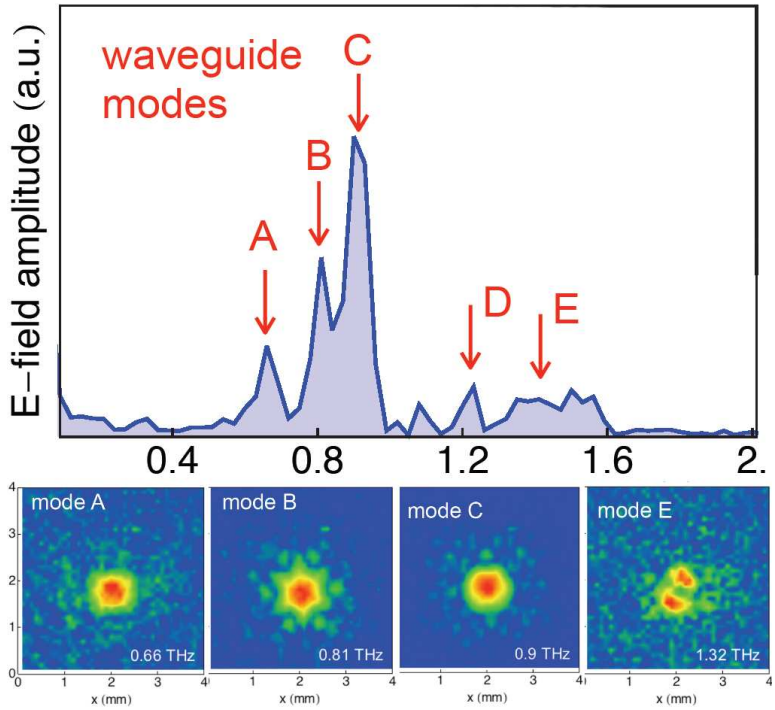

Figure 6.6: Near-field measurements of the Topas hollow core fiber.

of $2\pi\frac{f}{c}\Lambda = 9.5$. Due to the lower hole to pitch ratio requirement an attempt is made at making a hollow core PMMA THz fiber, despite the high bulk material loss of PMMA.

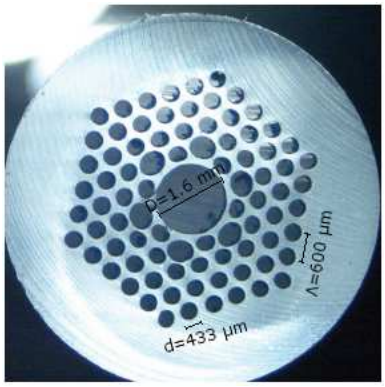

Figure 6.7: Image of the PMMA hollow core THz fiber.

In an effort to avoid the destructive expansion of the central hole experienced in the Topas hollow core fiber the PMMA fiber was drawn under conditions that will not cause large hole expansion. The preform was drilled in the same pattern as the Topas hollow core THz fiber. The resulting fiber is seen in Fig. 6.7. The fiber is 8.5 mm in diameter and as such is slightly thicker than the Topas fiber. The cladding structure is homogenous and there is no apparent chirp. The pitch of the cladding is 600 µm and the average hole diameter is 433 µm; the holes have experienced no, or very little, hole expansion. The core diameter is 1.6 mm. The hole to pitch ratio is 0.72, not optimal, but high enough to cause bandgaps according to the calculations reported by Pottage *et al.*[54]. The bandgap should be centered at approx. 750 GHz and have a width of only 60 GHz. Similarly as the case is with the Topas hollow core THz fiber, there may exist frequency ranges of low cladding mode density. The fiber is investigated in the terahertz time-domain spectroscopy (THz-TDS) setup.

The time traces through 3 different lengths of PMMA hollow core THz fibers are shown in Fig. 6.8 together with the reference measurement. The transmitted radiation is noticeably weaker than the reference indicating low efficiency. What is interesting is that the time traces look almost identical for all three lengths; there is a very small time delay of only a few ps between the transmitted radiation and the reference. All three PMMA hollow core fiber lengths are longer than the Topas fiber and the refractive index of PMMA is larger than that of Topas; thereby the delay should be larger than the delay experienced by the Topas hollow core fiber. The only possible explanation that the delay is not larger is that almost all of the radiation is traveling in air. The same conclusion can be reached by observing the

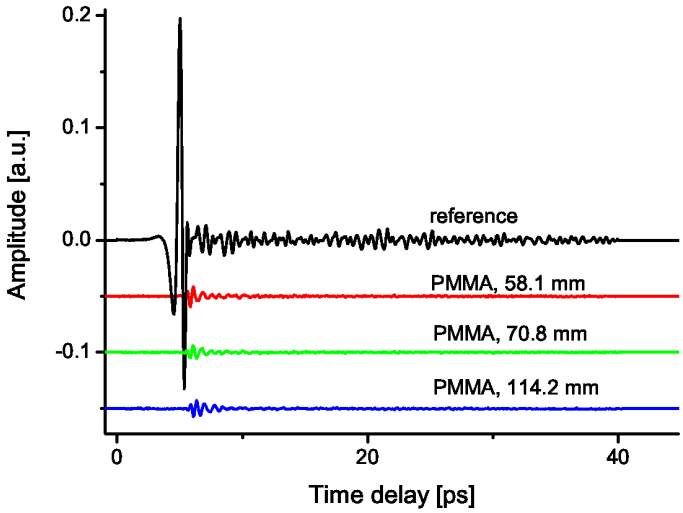

Figure 6.8: Time trace of the THz transmission through 3 different lengths of the PMMA hollow core fiber. Note the plots are offset for clarity.

amplitude of the transmission. The absorption of PMMA is 50 times higher than the absorption of Topas; at the transmitted frequencies the absorption coefficient is larger than 10 cm^{-1} as seen in Fig. 2.5. Since the amplitude of the transmitted radiation is not affected by almost doubling the PMMA fiber length, the conclusion must be that the radiation is not transmitted through PMMA. The frequency components of the transmitted THz radiation are shown in Fig. 6.9. The transmission range starts at around 1 THz and stretches to well above 2.5 THz. The end of the transmission band is difficult to detect because of the falling off of the setup bandwidth. There is not much detectable difference between the three transmission spectra, suggesting low attenuation. Although the calculations on this structure offer the possibility of frequency ranges of low mode density similarly to the Topas hollow core fiber, the low density ranges can not be this wide.

The spectrogram from transmission in the three PMMA hollow core THz fiber lengths is shown in Fig. 6.10. The difference between the three transmissions is not large, however it seems as if the transmission through the longest fiber is arching more than the transmission through the shortest fiber. This indicates that there is some dispersion. This dispersion could be waveguide dispersion or it could be modal dispersion. The temporal splitting and width of the pulse at low frequencies indicates that there could be more than one mode propagating through the fiber. This is particularly clear when comparing the short and the middle fiber. The spectrogram from

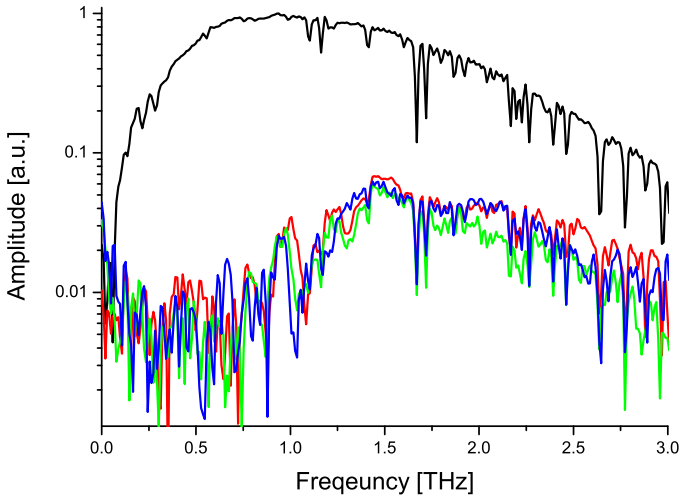

Figure 6.9: Frequency components of the THz radiation transmitted through the PMMA hollow core fiber. Color code is the same as in Fig. 6.8

the long fiber is not as wide at low frequencies. This could be because the higher order modes have larger attenuation than the fundamental mode. The transmission through the middle length fiber is different from the other two, both in bandwidth and in amplitude and is probably due to coupling issues.

6.2.1 Near-field measurements

The three PMMA hollow core THz fibers were also sent to the University of Freiburg for near-field measurements. In Fig. 6.11 the input frequency distribution is shown together with the output frequency distribution from the PMMA hollow core THz fiber. In Fig. 6.12 the transverse field distribution at 0.98 THz is shown. Unfortunately the near-field measurement setup at the University of Freiburg has a smaller bandwidth than than the one used in our lab. Therefore the measurements at Freiburg only show the lowest frequency part of the transmission up to around 1.6 THz. However the measurements from Freiburg still complement our measurements, as they confirm the transmission through the fiber and they prove that there is a core mode propagating through the fiber.

The loss of the PMMA hollow core fiber has also been measured to 1.13 dB/cm at 1.5 THz. The loss measurement is based on only three fiber lengths, therefore the confidence in this figure is not very high. A loss figure of 1.13 dB/cm would mean that the transmission difference between

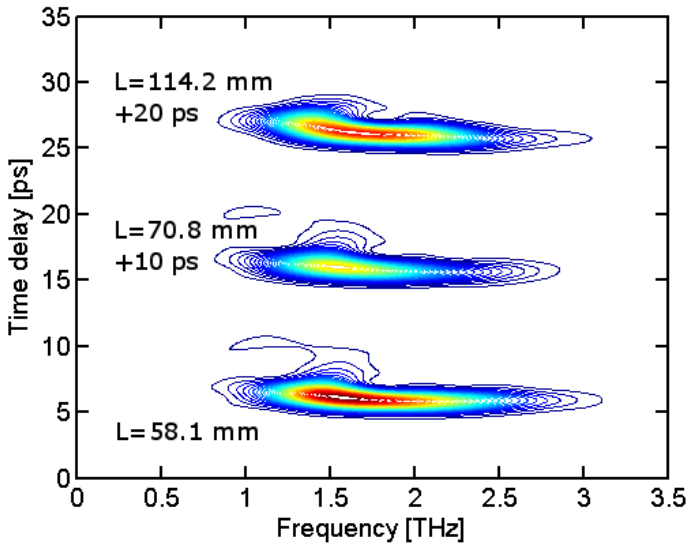

Figure 6.10: Frequency components of the THz radiation transmitted through the PMMA hollow core fiber.

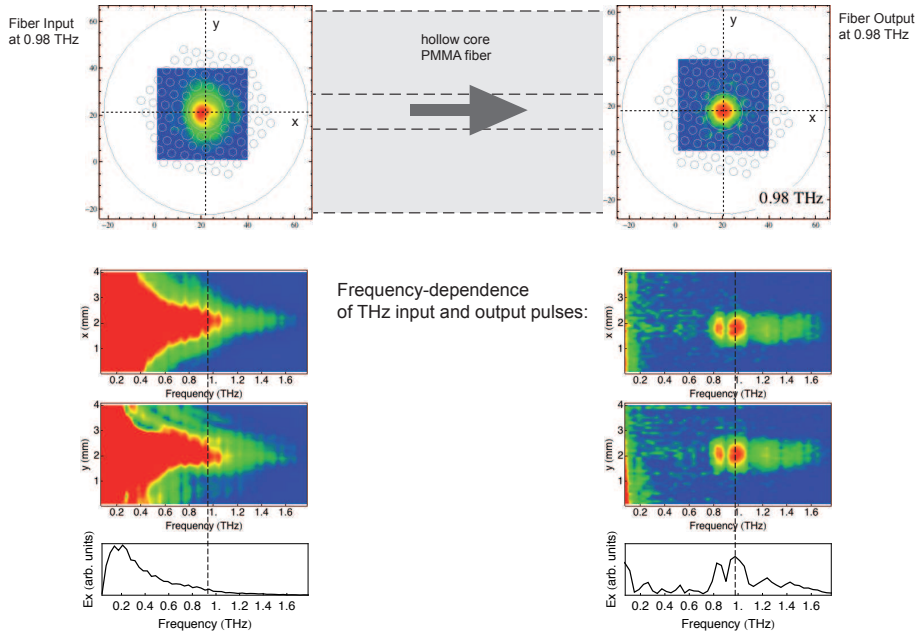

Figure 6.11: Near-field measurements of the THz field at the input of the fiber and at the output.

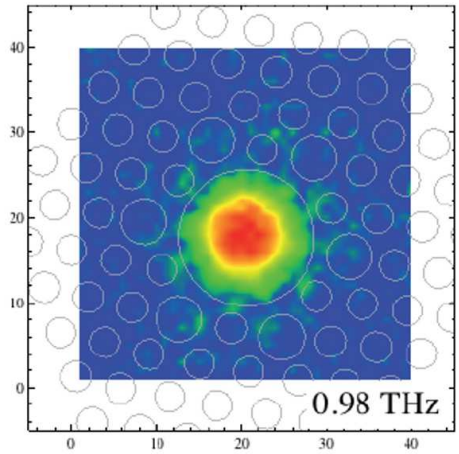

Figure 6.12: Near-field measurement of the PMMA hollow core THz fiber at 0.98 THz. The structure of the fiber is overlayed on to the measurement.

the shortest fiber and the longest fiber is 5.5 dB, in our transmission measurements we can not see this big a difference. The reason we can not see the loss could be because the longer fiber compensates for the loss by being closer to the receiver antenna. However it would be an unlikely event that this compensating effect would exactly outweigh the propagation loss.

6.2.2 Numerical calculations

The PMMA hollow core THz fiber is also investigated numerically to identify what guiding mechanism is responsible for the transmission through the core. A quarter domain model of the fiber is built in COMSOL and solved for modes around the airline using the refractive index of PMMA shown in Fig. 2.5 using second order polynomial to extrapolate to high frequencies, the extrapolation was checked against the data in Fig. 2.4, this figure includes the properties of PMMA at higher frequencies. The mode density of all the modes that have an overlap with the structured part of the fiber that is larger than 40% are shown in Fig. 6.13. In the same figure the modes that have a overlap with the core that is larger than 80% are plotted with red circles. As expected there is no apparent bandgap. A bandgap would manifest it self as blank region in the middle of a high mode density area. The white regions in the figure are due to there not being any calculated modes in that area. This is not a consequence of the fiber design, but simply because the mode solver has not searched for modes in this area. The discontinuity in the mode density from 1 THz to 2 THz is caused by the combination of two separate calculations.

The modes with a overlap with the core larger than 80 % could possibly

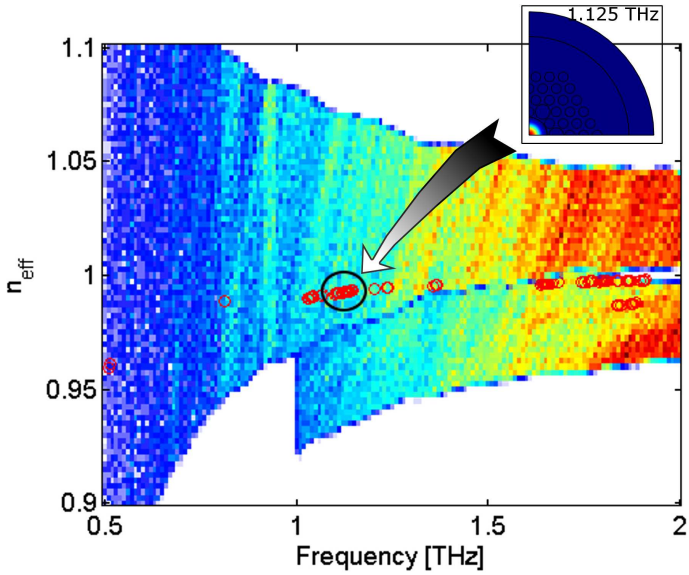

Figure 6.13: Calculated mode density for the PMMA hollow core fiber without including material loss. Red circles represent modes that have a overlap fraction with the core that is larger than 80 %.

be guided in the core, one required feature of the core mode is that it has low attenuation. The effective material loss of the fiber α_{eff} can be estimated using [56]:

$$\alpha_{\text{eff}} = \frac{(\epsilon_0/\mu_0)^{1/2} \int_{A_{\text{mat}}} n\alpha_{\text{mat}} |\mathbf{E}|^2 \mathrm{d}A}{\mathrm{Re}\{\int_{A_{\text{all}}} \mathbf{E} \times \mathbf{H}^* \cdot \mathbf{z} \, \mathrm{d}A\}} = \alpha_{\text{mat}}\eta \tag{6.1}$$

where Re denotes the real part, n is the refractive index of the material, α_{mat} is the material loss. $\mathbf{E}$ is the electric field component and $\mathbf{H}^*$ is the complex conjugated magnetic field component. $\mathbf{z}$ is the unit vector in the z-direction. The integration in the numerator is only performed over the solid material (A_{mat}) since the propagation loss of THz radiation in air is negligible. As the material loss is spatially uniform, the effective loss (α_{eff}) is given by the product of the material loss and the fraction of power in the material (η). If the material loss is low then the low loss approximation can be applied such that the field components used in the integrals are calculated for a structure with no loss. The bulk loss is extrapolated in a similar way as the refractive index. The calculated material loss together with the calculated confinement loss of the modes that have 80% overlap with the core are shown in Fig. 6.14.

Although the narrow ranges of core modes exhibit propagation loss that is much smaller than the loss of bulk PMMA, these results do not explain the observation in the experiments. The lowest calculated loss above 1 THz

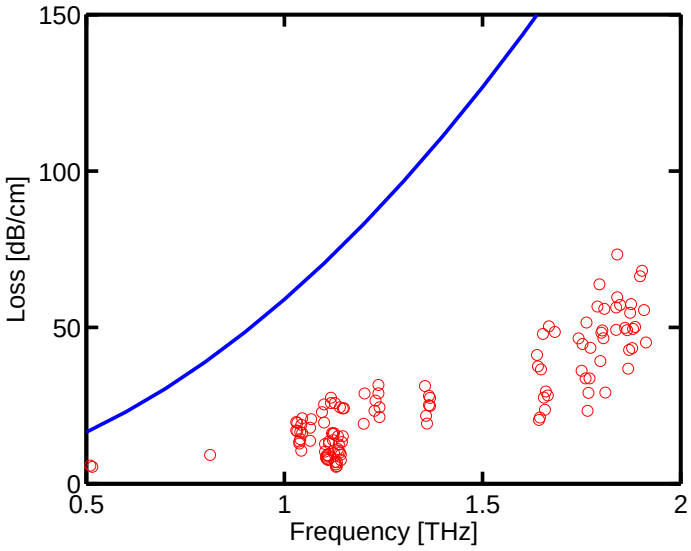

Figure 6.14: Numerically calculated attenuation of the modes with a core fraction larger than 80 %. The blue line indicates the bulk material loss of PMMA.

is 6.2 dB/cm resulting in a loss of 31 dB for a 5 cm long fiber. Measurements have shown that the loss is undetectable between the fiber lengths 58.1 mm and 114.2 mm, an extra length of more than 5 cm. The conclusion is that the numerical modeling is not explaining the transmission. The model is apparently not realistic enough, possibly because the material loss of PMMA is too high to be ignored.
Although the material loss of PMMA is high, when converted into the imaginary part of the refractive index, it is less than 2% of the real part below 1 THz, and assuming extrapolation based on the measurement shown in Fig. 2.5, the fraction is only going from 2% to 4% between 1 THz and 2 THz. Could this fraction be enough to explain the transmission? In order to investigate the importance of the imaginary part of the refractive index, the calculations are repeated using the same real part but including an imaginary term representing material loss. The new mode density is shown in Fig. 6.15. This time the red circles represent modes with an overlap with the core that is larger than 90 %. The red circles start at around 1 THz and continue as far as the calculations have been performed. Already this result is much more similar to the experimental measurements as it indicates that there is a transmission window starting at around 1 THz continuing beyond 2 THz.

The total propagation loss of the fiber is much lower than that found when neglecting the imaginary term. This finding is in conflict with the

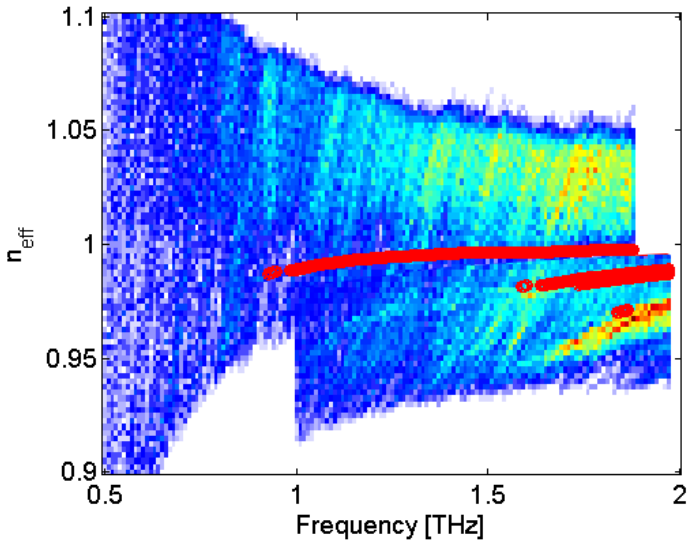

Figure 6.15: Numerically calculated mode density for the PMMA hollow core fiber including the bulk loss of PMMA. The red circles represent modes that have a overlap with the core that is larger than 90%.

Im/Re of n in %	1.72	3.44	6.88	13.76	27.52
attenuation [dB/cm]	2.59	2.16	1.78	1.51	1.37
n_{eff}	0.9963	0.9962	0.9962	0.9961	0.9961

Table 6.1: The relation between attenuation and effective refractive index of the core mode as the fraction of imaginary to real part of the refractive index of the material increases. The calculations are made at 1.5 THz.

calculation made using Eqn. 6.1; this conflict is caused by the assumption that the material is low loss. Increasing the imaginary part of the refractive index leads to better confinement of the core mode and lower propagation loss as seen in Tab. 6.1 (calculation made at 1.5 THz).

The PBG effect does not explain the wide transmission bandwidth seen in the measurements. One other possible explanation is inhibited coupling. However this kind of guiding usually shows abrupt transmission dips caused by mode crossing, this is not seen in the measurements. The last option is that this is similar to a tube waveguide, the light being uninfluenced by the surrounding structure. In order to check if this is the case, a tube waveguide with similar core size is numerically compared to the hollow core fiber. The two structures are shown in Fig. 6.16. The refractive index in both cases is almost the same as seen in Fig. 6.17. The main difference is that the hollow core fiber has a cut-off at around 1 THz where the tube waveguide continues to much lower frequencies.

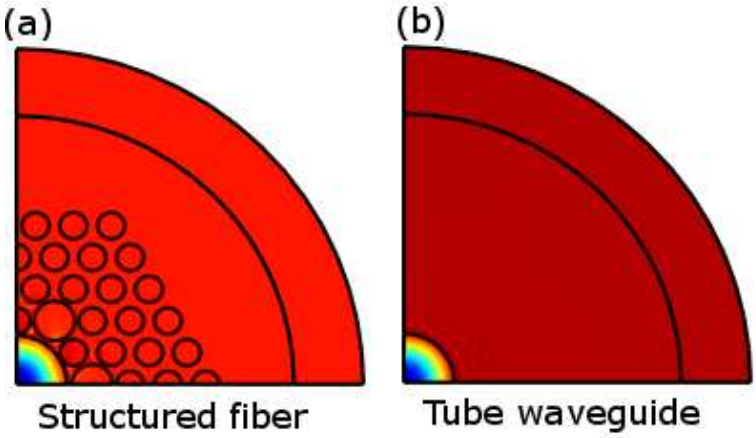

Figure 6.16: The COMSOL models of the hollow core fiber (a) and the tube waveguide (b). The fundamental core mode of both models at 1.5 THz is also shown.

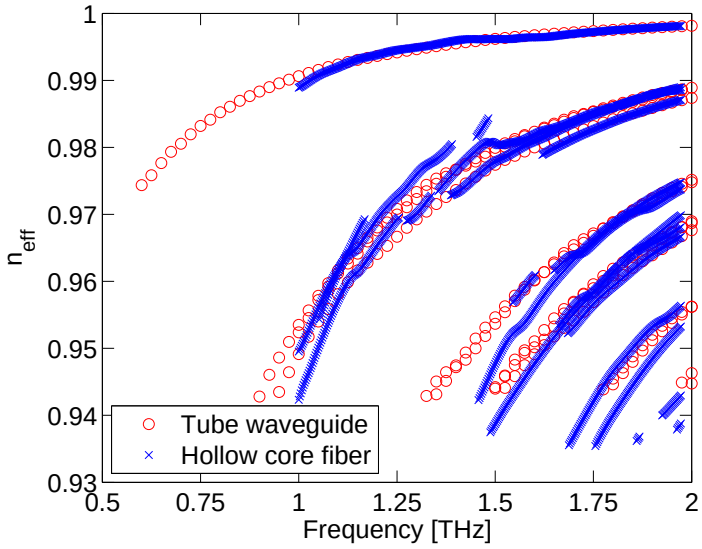

Figure 6.17: Calculated effective refractive index of the tube waveguide shown as red circles and the modes of the hollow core fiber shown as blue crosses. All the modes have an overlap with the core that is larger than 70%.

The total propagation loss of the calculated core modes is shown in Fig. 6.18. Interestingly the hollow core fiber has lower loss than the tube waveguide in some frequency ranges. This is especially apparent at around 1.1 THz where the hollow core fiber has a loss of 0.9 dB/cm while the tube waveguide has loss of 2.5 dB/cm, but it is mainly the higher order core modes that are influenced by the structure. The lowering of the loss as the frequency increases corresponds well to the results found by Issa *et al.*[57] when investigating tube waveguides in the optical domain. However they do not include loss, and according to their findings the confinement loss of this waveguide should be in excess of 50 dB/cm, again indicating that the inclusion of the imaginary term increases confinement.

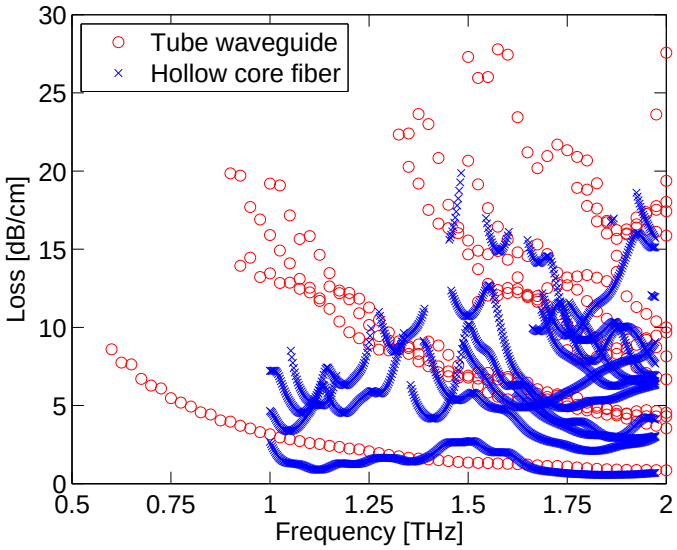

Figure 6.18: Numerically calculated total attenuation of all the modes with a core fraction larger than 70 %. Symbols are the same as in Fig. 6.17.

According to tube waveguide theory [58] the loss of the tube waveguide should decrease as the diameter of the core increases. This relation is numerically investigated and the results of the calculation performed at 1.5 THz is presented in Tab. 6.2. Interestingly the losses can be as low as 1 dB/m for a realistic waveguide design.

The influence of the imaginary term on the confinement of the radiation in a hollow core waveguide or a tube waveguide needs closer investigation. One possible explanation of the guiding mechanism is given in the paper by Kristensen *et al.*[59] where the authors theoretically demonstrate guidance based solely on imaginary refractive index. In the paper the authors find that in order for the core mode to couple to cladding modes the real and imaginary parts of the effective index have to match. To illustrate this, two

core diameter [mm]	0.8	1.6	3.2	6.4
attenuation [dB/cm]	12	1.7	0.2	0.01
n_{eff}	0.9832	0.9959	0.9988	$\tilde{1}$

Table 6.2: Propagation loss of the tube waveguide as the core size increases. The imaginary part of the refractive index is 1.72% of the real part.

maps are shown in Fig. 6.19, where the difference between the cladding modes and the core modes is more apparent. The distance on the map between the core mode and the cladding modes is related to the coupling. The further the core mode is away from the cladding modes the better confined the core mode is. The core mode in the map Fig. 6.19(a) at 1.125 THz is more isolated than the core mode at 1.5 THz. Comparing this to the propagation loss in Fig. 6.18 showing that at 1.125 THz the loss is lower than at 1.5 THz, it seems that there is a connection between the isolation on the map and the total propagation loss.

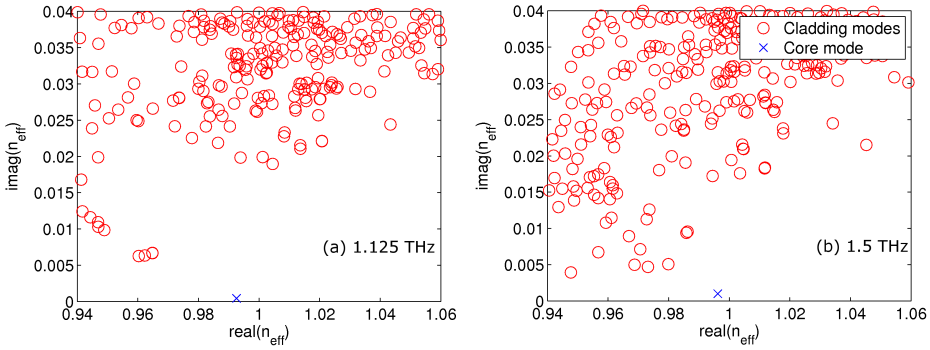

Figure 6.19: Two mode maps based on the calculated modes of the PMMA hollow core fibers calculated at 1.125 THz (a) and 1.5 THz (b). The position of the modes is plotted as a function of the real and imaginary parts of the effective index. Red circles represent the cladding modes, including some of the higher order core modes, the blue cross represents the fundamental core mode.

The introduction of the imaginary term into the calculations opens up new design possibilities, where the freedom of design is increased since PMMA fibers can be manufactured in more complex shapes than with materials typically used for tube waveguides, such as metal tubes [18] or metal coated silica tubes [29].

6.3 Porous core honeycomb band gap THz fiber

To overcome the fabrication problems of differently sized holes in the hollow core THz fiber, a novel porous-core honeycomb bandgap design is investigated. The holes of the porous-core are the same size as the holes in the surrounding cladding, thereby giving the proposed fiber important manufacturing benefits. The fiber is studied theoretically. The fiber is shown in the following to have a 0.35 THz wide fundamental bandgap centered at 1.05 THz and a calculated minimum loss of 0.25 dB/cm.

The bandgap fibers are typically designed using a tightly packed triangular structure where the holes are highly inflated to give a high air-fill fraction. The high air-fill fraction in combination with a large air defect in the core is needed in order to achieve an efficient and broad bandgap [42]. Honeycomb bandgaps are relatively larger than triangular bandgaps and at comparable structure sizes the honeycomb bandgap is at lower frequencies than the triangular bandgap [60], which can be exploited to make a thinner fiber. The thickness of the fiber is one of the factors limiting the applications of THz fibers. In order to be flexible and compact the fiber should be as thin as possible.

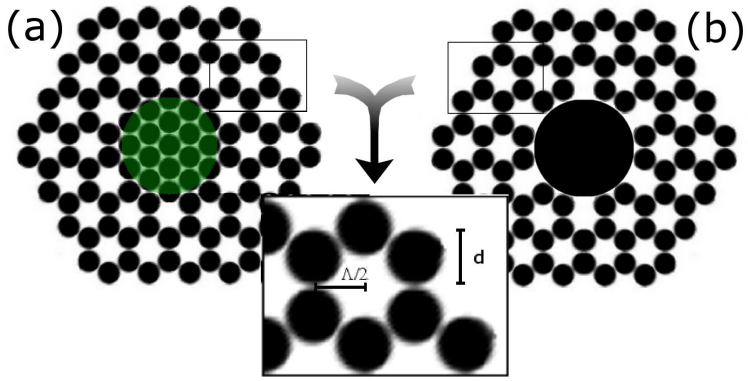

Figure 6.20: Honeycomb fiber with (a) 7-hole porous-core and (b) a 7-cell hollow core. Dark regions represent air.

The honeycomb bandgap fiber designs are shown in Fig. 6.20. In the porous-core fiber all the holes have the same diameter d. In the hollow-core fiber the core is created by removing 7 honeycomb cells, resulting in a hollow core of the same size as the effective core of the porous-core fiber.

The fiber is considered to be made of Topas. The structure is chosen to have a pitch of Λ =250 μm and hole to pitch ratio of d/Λ =0.55 as this results in a fundamental bandgap near 1 THz. The bandgap of the cladding unit cell is calculated using MPB. The resulting bandgaps are shown in gray in Fig. 6.21. In order to take the finite cladding structure into consideration

the calculations on the fiber with core defect are made using COMSOL. The fundamental core mode of a 4-ring fiber for both bandgaps is also shown in Fig. 6.21. Since the COMSOL modeled fibers have a finite cladding size, the resulting bandgap is different from the one found using MPB. Therefore some of the core modes extend slightly outside the bandgap indicated in gray in Fig. 6.21. In order to define the core mode the fraction of power in the core is calculated. The core is defined as a circle of radius 300 μm. The dashed curves in Fig. 6.21 represent modes with a fraction of power in the core larger than 55% while the solid line represents an overlap larger than 25%. The second bandgap has several higher-order core modes. These are not included because they all lie close to the bandgap edge, making them sensitive to perturbations and therefore unfit as guiding modes.

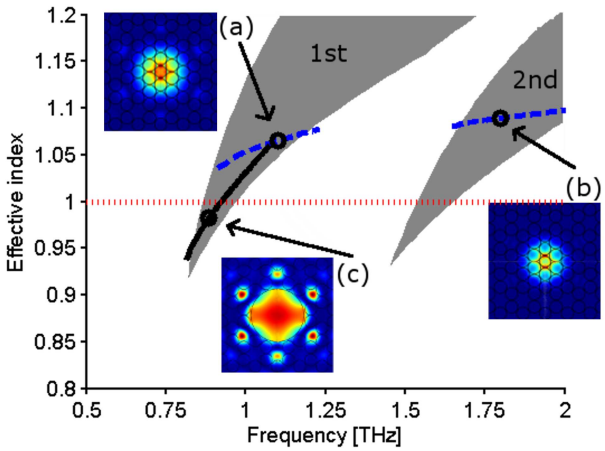

Figure 6.21: The calculated bandgap is shown in gray, the effective indices of the core mode of the porous fiber are shown as blue dashed curves and the effective index of the core mode of the hollow core fiber is shown as solid black curve. The dotted straight line indicates the air line. The insets show modes of the porous fiber at 1.1 THz(a) and 1.8 THz(b), and the mode of the hollow core fiber at 0.885 THz(c).

The bandgaps only dip below the airline in a narrow frequency range due to the low air filling fraction. Even so, the hollow core fiber supports a guided mode in the first bandgap. However this mode has most of the field guided in the six rods closest to the core, as seen in Fig. 6.21(c). This leads to a low fraction of power in the core. Consequently the mode cutoff for the hollow core fiber is defined as when the fraction of power in the core is less than 25%. Even though the 2nd bandgap also dips below the air line the hollow core fiber does not support any core mode in the 2nd bandgap. The slope of the mode lines in Fig. 6.21 indicate that the porous-core fiber is less dispersive than the hollow core fiber and they also show that the porous-core

fiber has a wider transmission window than the hollow core fiber.

The behavior of the fundamental core mode is dependent on the extent of the cladding. In order to investigate this relation in more detail we consider cladding sizes of 2, 3 and 4 rings for the porous-core fiber. The fraction of power in the core in the first bandgap of the three cases is shown in Fig. 6.22(a). The 4-ring fiber (dashed) gives the most clean bandgap, whereas the 2 (dash-dotted) and 3 (dotted) ring fibers have large confinement dips in the bandgap. The hollow core fiber (solid black curve) has a 4-ring cladding and confines the field poorly to the core. A 4-ring fiber with the given pitch would result in a 3 mm thin fiber, half the thickness of a previously reported THz Bragg fiber [30].

The effective material loss of the fiber α_{eff} can be estimated using Eqn. (6.1). The low loss approximation is applied so that the field components used in the integrals are calculated for a structure with no loss. The resulting η is shown in Fig. 6.22(b), which shows that in the middle of the porous-core fiber bandgap the effective loss is approaching 20% of the bulk loss. The bulk loss at 1 THz is 1 dB/cm giving an effective loss of $\alpha_{\text{eff}} = 0.20$ dB/cm.

A second loss mechanism in fibers is confinement loss. This loss is normally much smaller than the material loss, but at the bandgap edges it becomes significant. Using COMSOL it is possible to model a realistic fiber and by applying a perfectly matched layer around the fiber with a refractive index of 1 (air) the confinement loss can be calculated. In Fig. 6.23 the confinement loss is added to the effective material loss to produce the total loss for the 4-ring fibers. The material loss is the measured bulk loss of Topas, shown as red circles. The polynomial fit used in the calculation is shown as a red dotted line.

At the edges of the bandgap the confinement loss increases for both fibers and the confinement loss is also large in the ranges where the fraction of power in the core is low. Even though the hollow core fiber supports a mode confined to the low loss air core, a large part of the power is still propagating in the material, giving a high effective loss. Additionally the hollow core fiber is seen to suffer from excessive confinement loss. The porous-core fiber also supports a mode in the second bandgap with losses at around 0.5 dB/cm.

The fiber has been fabricated and will be investigated using THz-TDS in the near future. An image of the fabricated fiber is shown in Fig. 6.24.

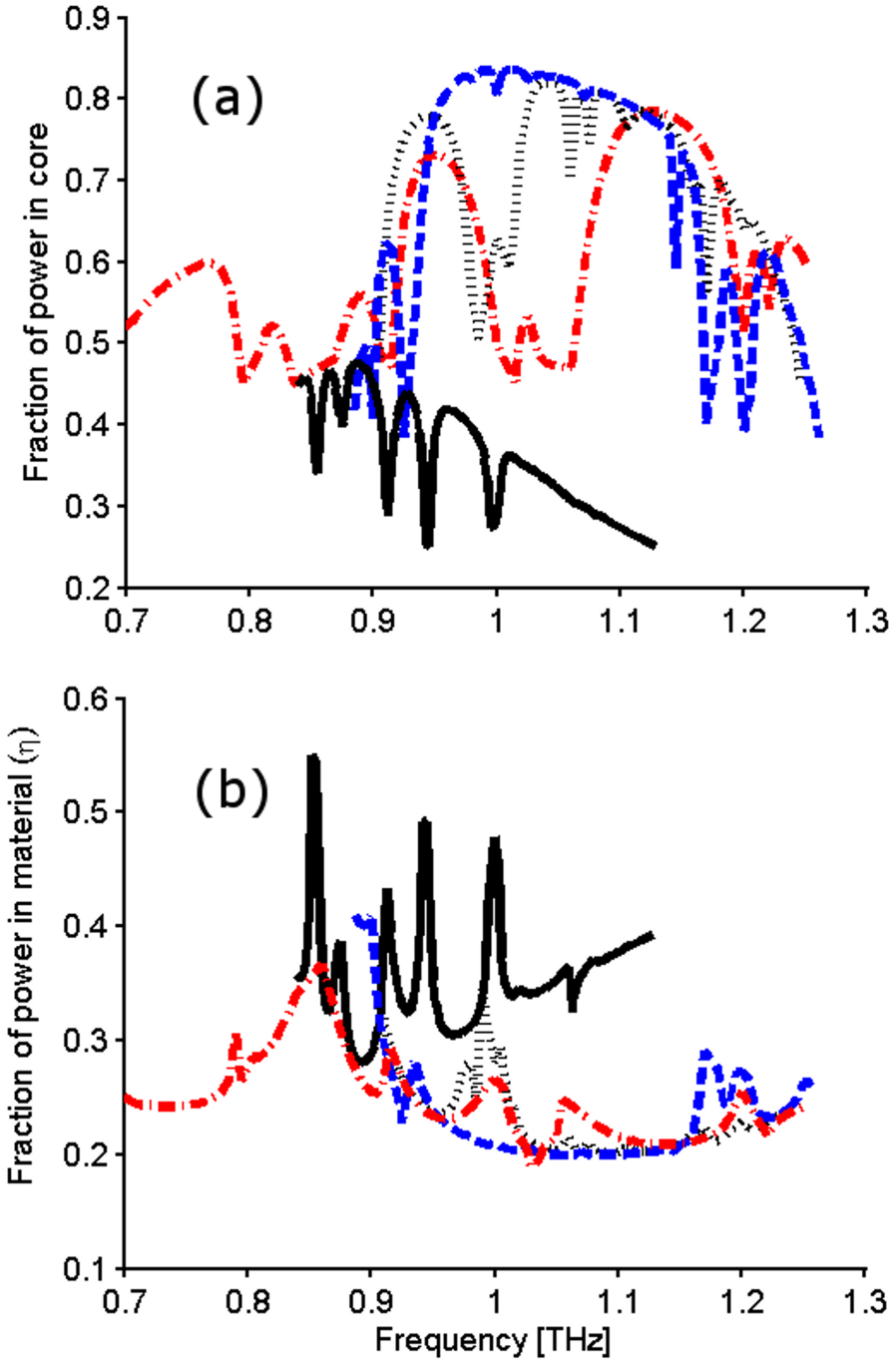

Figure 6.22: (a) Fraction of power localized in the core of the fiber for 2-ring (red dash-dot), 3-ring (black dottet) and 4-ring (blue dashed) porous-core fibers and the hollow core (black solid) fiber. (b) Calculated fraction of power in the material (η) for all fibers.

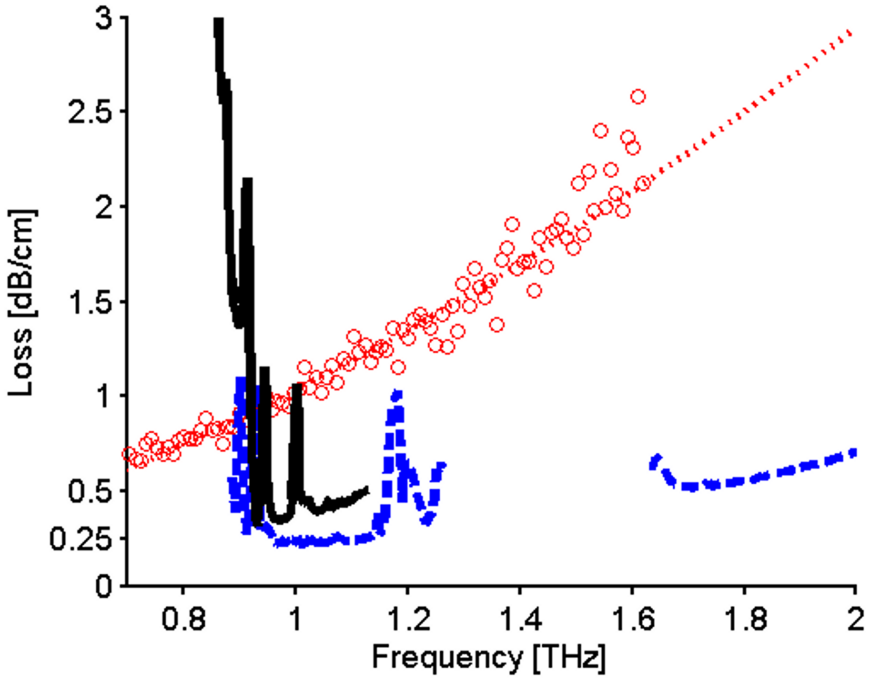

Figure 6.23: Total loss of the porous-core (blue dashed) and hollow core (black solid) 4-ring fibers. Bulk loss is shown as red circles and the polynomial fit to the bulk loss is shown as a red dotted line.

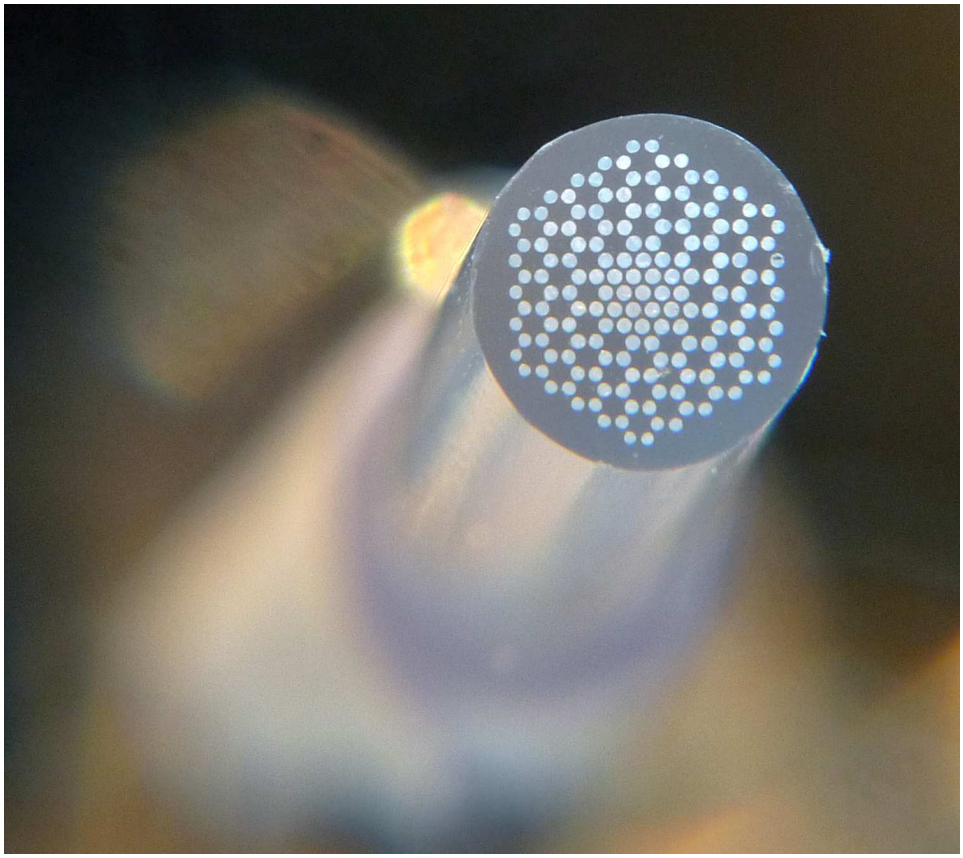

Figure 6.24: Image of the manufactured honeycomb THz bandgap fiber.

Chapter 7

Broadband 3-dB coupler

As an example of a THz polymer fiber device, the design of a short length broadband fiber directional coupler for terahertz (THz) radiation is investigated in this chapter. A 3-dB coupler device with a bandwidth of 0.6 THz centered at 1.4 THz is demonstrated theoretically. The broadband coupling is achieved by mechanically down-doping the cores of a dual-core photonic crystal fiber by microstructuring the cores. This is equivalent to chemical down doping but easier to realize experimentally.

A THz directional coupler has been previously reported [27], where the coupling was achieved by placing two fibers in close proximity. However, both fibers were sub-wavelength sized rod-in-air type fibers [19, 24–28]. The advantage of such a rod-in-air fiber is that the THz field has a small overlap with the lossy waveguide material. However, these fibers have the disadvantage that they are difficult to handle, since any contact on the surface disturbs the field and leads to large scattering loss.

7.1 Device description

The structure of the investigated device is shown in Fig. 7.1. The down-doped cores experience mode field diameter minima, leading to frequency ranges of constant coupling lengths, as suggested by Lægsgaard *et al* [61]. In addition to broadband coupling the proposed coupler also has a short coupling length, which is a necessary property considering that the material loss is high in the THz regime.

The coupler is made as a dual-core photonic crystal fibre (PCF) using Topas as the background material. The proposed fiber has a pitch (Λ) of 750 μm and a hole diameter (d) of 300 μm, giving a hole diameter to pitch ratio (d/Λ) of 0.40. The fiber has two cores separated by a center to center distance of twice the pitch. In each core there is a region that is mechanically down-doped by a triangular microstructure air hole structure with a pitch Λ_c and hole diameter d_c as seen in Fig. 7.1.

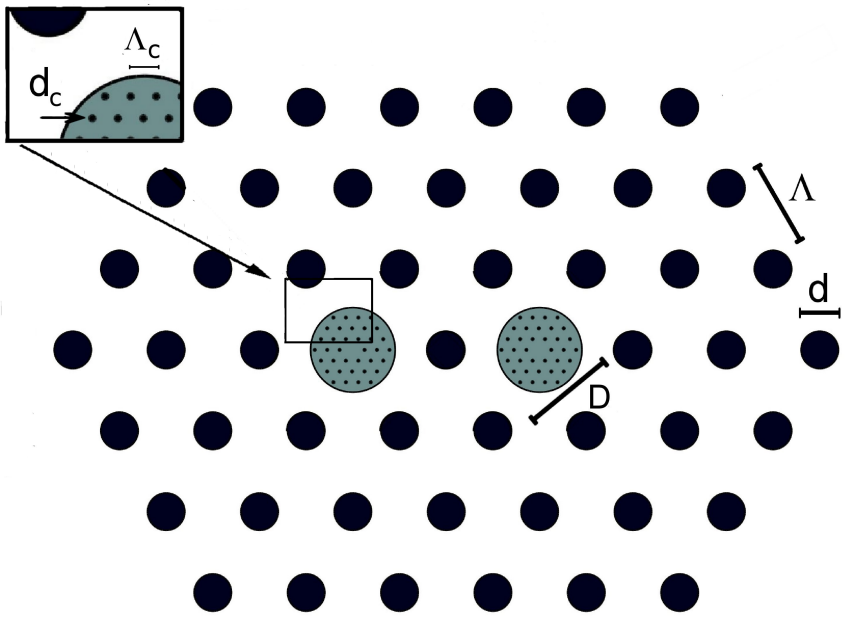

Figure 7.1: Broadband THz coupler design with mechanically down-doped cores. All the considered designs have pitch $\Lambda = 750$ μm and hole to pitch ratio $d/\Lambda = 0.40$

The dual-core fiber will support two fundamental modes for each polarization, one even and one odd mode. The difference in propagation constant between these modes gives the coupling length. For simplicity only the results of one polarization are presented. The coupling length is the length required before achieving a π phase change between the two modes, $L_c = \frac{\pi}{|\beta_e - \beta_o|}$, where β_e and β_o are the propagation constants for the even and odd modes, respectively. The effective refractive index of the core modes is calculated using MPB, with a $9\Lambda \times 9\frac{\sqrt{3}}{2}\Lambda$ supercell using 600×600 grid points.

7.2 Numerical calculations

The fiber parameters affecting the coupling length are the pitch, the hole size, the size of the doped region, and the dopant level. The pitch and hole size are fixed.

Given that the structure is designed to be endlessly single mode it does not support any higher order modes. The fiber guidance is however limited by two factors. For frequencies below 0.3 THz the wavelength of the radiation is too large to be confined efficiently to the core and the confinement loss rises rapidly. At very high frequencies the waveguide is sensitive to bending

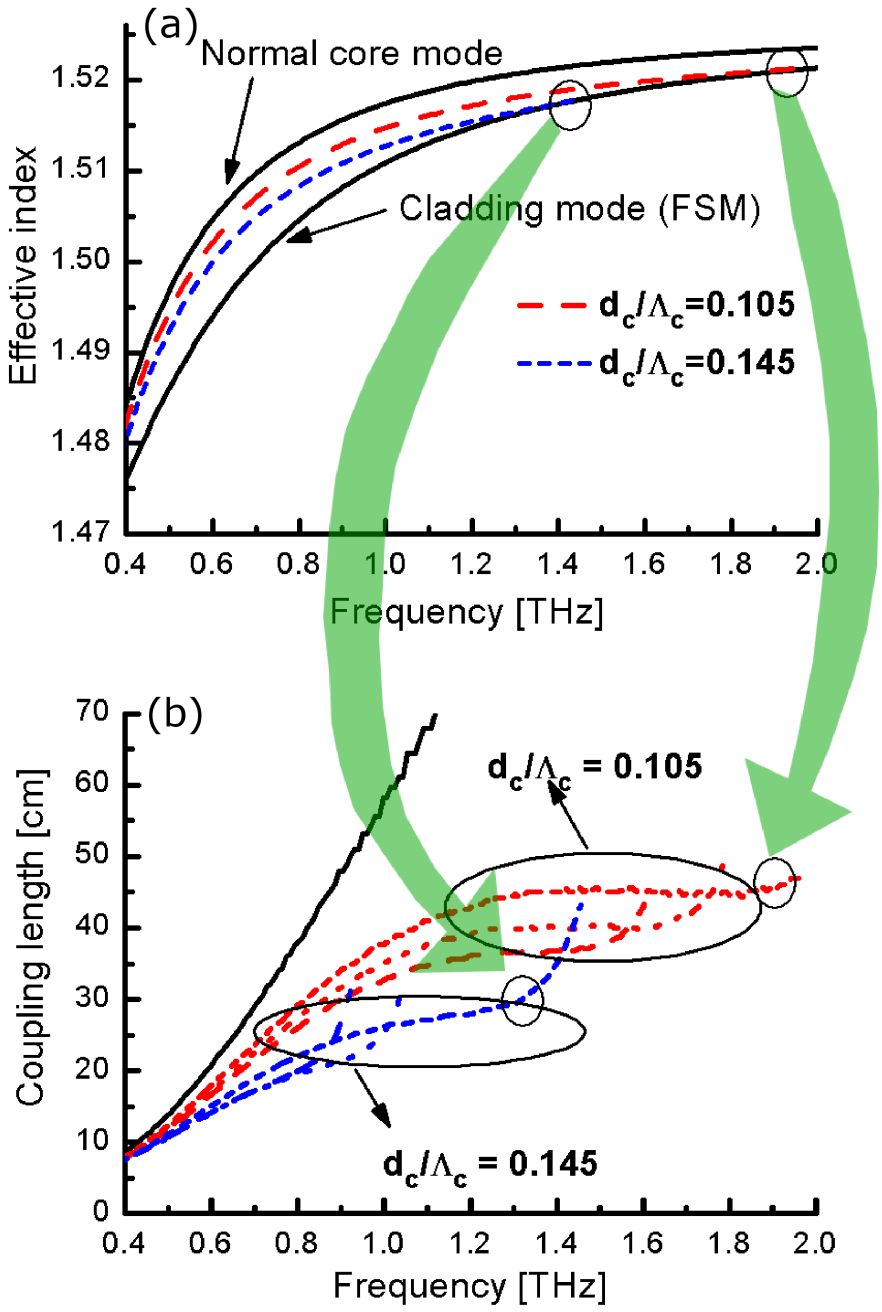

Figure 7.2: (a) Effective refractive index of the odd modes of doped coupler designs with Λ_c=97.5 μm, d_c/Λ_c=0.105 (red long dash) and d_c/Λ_c=0.145 (blue short dash). The top solid line (black) is the index of the odd mode of the undoped core coupler while the bottom solid line (black) is the fundamental space filling mode (FSM). (b) Coupling length of a normal coupler (solid) and down-doped couplers (dotted and dashed). Red lines have Λ_c=97.5μm (short dash), Λ_c=108.75μm (dotted) and Λ_c=120μm (long dash). Blues lines have Λ_c=97.5μm (short dash), Λ_c=127.5μm (dotted) and Λ_c=150μm (long dash). The large green arrows indicate where the cut-off of the odd mode in (a) leads to an abrupt increase in the coupling length in (b).

and handling since the core mode is highly sensitive to micro bending [53]. The high frequency cutoff of the waveguide with an undoped core is not relevant in this work. However, as we down dope the core of the coupler we shift the high frequency cutoff of the core modes to lower frequencies. This is illustrated in Fig. 7.2(a) where the effective refractive index of the odd mode is plotted together with the fundamental space-filling mode (FSM). The effective index of the modified cores crosses the FSM at 1.9 THz for d_c/Λ_c=0.105 and at 1.3 THz for d_c/Λ_c=0.145, where Λ_c=97.5 μm. This crossing coincides with the sudden increase in the coupling length seen in Fig. 7.2(b). As the frequency approaches this crossing the core modes will start coupling with cladding modes. We define the bandwidth B of the cou-

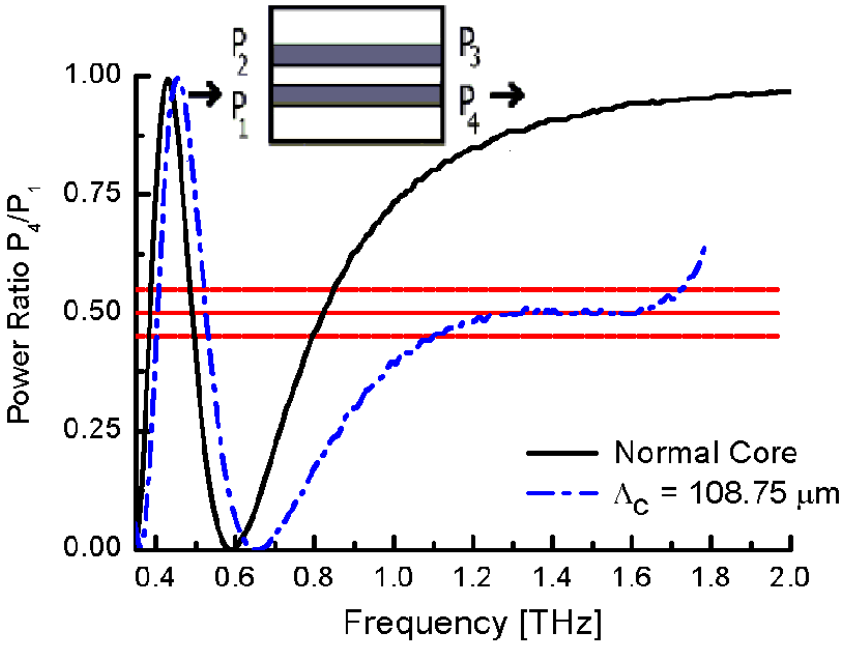

Figure 7.3: Normalized output from the launch arm of a 20 cm long coupler. The undoped coupler (solid) crosses the 50% region rapidly and therefore has a narrow bandwidth. The microstructured coupler has a plateau around 50% centered at 1.4 THz and therefore has a broad bandwidth at 1.4 THz. In this case; d_c/Λ_c=0.105.

pling as the frequency range where the coupling length is the same within ±5%. Apart from the bandwidth requirement, the coupler should also be short, because the inherent material loss is high in the THz regime, even for Topas. The coupling length is shown in Fig. 7.2(b), for a normal coupler, and for six mechanically down-doped couplers. The three mechanically down-doped couplers that have a flat plateau at high frequencies all have the same hole to pitch ratio of d_c/Λ_c=0.105 while the three mechanically

down-doped couplers that have a flat plateau at low frequencies all have a hole to pitch ratio of d_c/Λ_c=0.145. In general we can state that the coupler with large d_c/Λ_c have the shortest coupling length while the couplers with the small d_c/Λ_c have the broader bandwidth. Thus a dual-core fiber

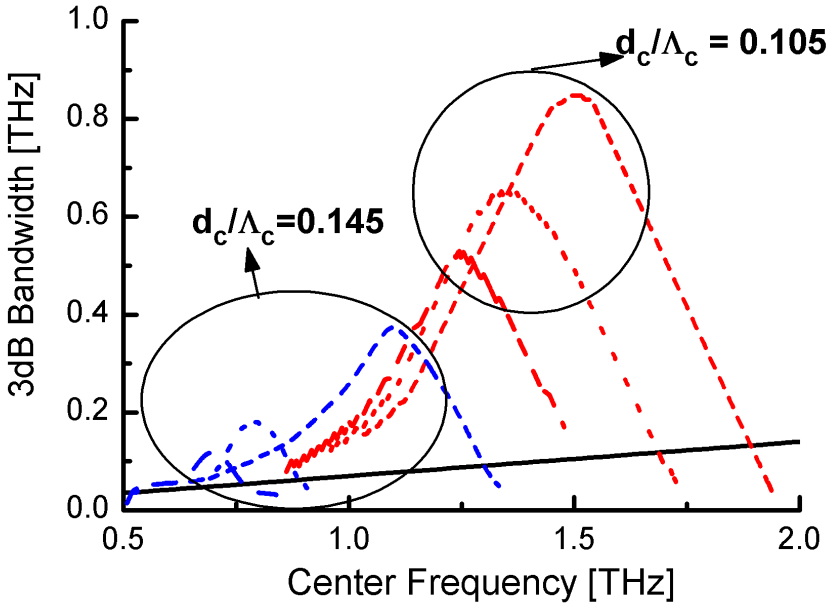

Figure 7.4: 3dB bandwidth vs. center frequency. The solid line (black) is the undoped coupler. The three high frequency designs (red) have d_c/Λ_c=0.105 while the three low frequency designs (blue) have d_c/Λ_c=0.145. In the high frequency case, the short dashed line has Λ_c=97.5μm, the dotted line has Λ_c=108.75μm and the dashed line has Λ_c=120μm. In the low frequency case, the short dashed line has Λ_c=97.5μm, the dotted line has Λ_c=127.5μm and the dashed line has Λ_c=150μm.

of this design with two microstructured cores with a pitch of 108.75 μm and d_c/Λ=0.105 can be used as a 3dB coupler centered at 1.4 THz, provided the fiber is 20 cm long corresponding to half the coupling length L_c.

7.3 Considering loss

The fraction of power at the output of the launch arm (P_4), see Fig. 7.4, of both a down-doped coupler and an undoped coupler for this device length is shown in Fig. 7.3. The fraction of power at the output of the launch arm is given by P_4/P_1=$\cos^2(L_d/L_c \cdot \pi/2)$, where L_d is the device length and L_c is the coupling length. From Fig. 7.3 it is clear that the down-doped coupler has a much broader 3-dB bandwidth than the normal coupler and also at

a higher frequency for the same device length. If the normal coupler was to have the same center frequency the device length would have to be more than twice as long.

The 3-dB bandwidth versus center frequency is shown in Fig. 7.4 for a lossless coupler. The d_c/Λ_c=0.105 couplers have the broadest bandwidth because their high frequency cut-off lie on a more flat part of the FSM curve seen in Fig. 7.2(a). However, the loss is neglected and these couplers have the longest device length of around 20 cm, so despite the broad bandwidth they might not be the best.

In order to take into consideration both the bandwidth B and the material loss $\alpha(\omega)$, a figure of merit is defined: FOM=$\frac{B}{\alpha(\omega)L_d}$. A large FOM requires now both a short device length and a broad bandwidth. It is important to keep in mind that the material loss is frequency dependent, and that in the THz range of interest, the loss rises almost linearly with frequency. The calculated FOM is shown in Fig. 7.5 where it now becomes clear how crippling the material loss is. Now the low frequency couplers are better than the high frequency ones and at very low frequencies (<0.6 THz) the normal coupler even has the best figure of merit. As previously stated the same results can be achieved by chemical down doping. To get comparable results as, for example, the Λ = 108.75μm coupler a circular region with diameter D = 0.88×Λ in the center of the two cores must be down-doped by 0.5%.

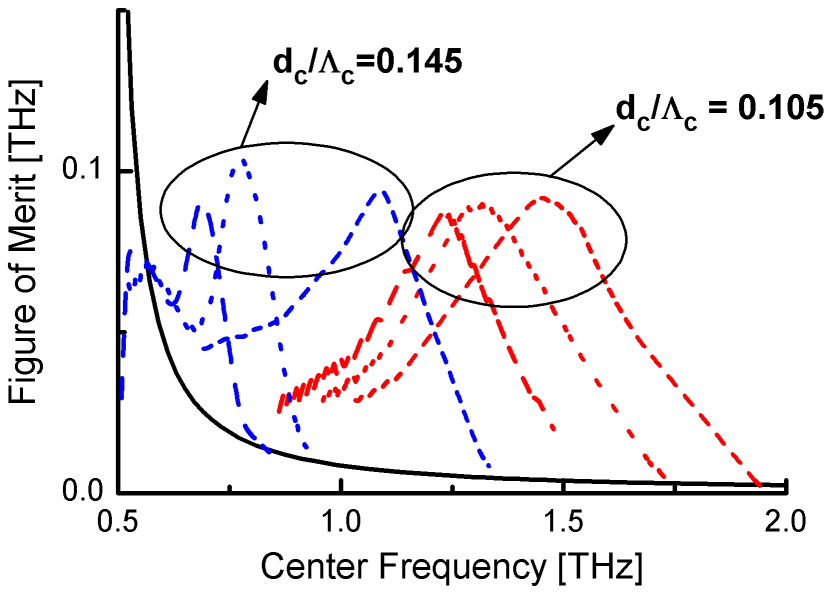

Figure 7.5: Figure of merit arranged as in Fig. 7.4.

Chapter 8

Conclusion

8.1 Summary

Structured polymer fibers have been investigated as terahertz (THz) waveguides. Two different types of fibers have been investigated, the solid core fibers and the hollow core fibers. The solid core fibers are demonstrated to have a dispersion that can be tailored by adjustment of hole diameter and pitch, and dispersive propagation has been demonstrated in a (Small Mode Area (SMA)) fiber as well as low dispersion propagation in a (Large Mode Area (LMA)) fiber. With a cut-back measurement the loss in the LMA fiber have been determined and found to be lower than 0.4 dB/cm; significantly lower than the material loss of the polymer material. The tight confinement of the guided mode to the solid core of the fiber allowed for low-loss propagation through a 90° bend of the fiber. Nearfield measurements of the profile of the propagating modes in the two fibers demonstrated single-mode operation of the LMA fiber, tight confinement of the guided mode to the solid core of the fibers, and the onset of propagation in an effectively microporous environment at low frequencies, most prominently observed in the SMA fiber with large hole to pitch ratio.

The second type of fiber that has been investigated is the hollow core fibers. Both Topas and PMMA fibers have been investigated and shown to propagate THz radiation in an air core at the center of the fibers. The fibers are shown not to work by means of the photonic bandgap mechanism, but rather by a mechanism similar to inhibited coupling. The PMMA fiber showed some surprising qualities and offers potential of very low loss as a THz waveguide. The numerical model of the PMMA fiber was found not to fit with experiments unless it included the high material loss of the material. The propagation loss decreases as the material loss increases, and numerical calculation have also shown that increasing the size of the air core will lower the loss, for a realistic fiber the loss could be as low as 1 dB/m.

A honeycomb bandgap fiber has also been designed and investigated, it

has been investigated as both a porous-core and a hollow-core honeycomb bandgap fiber. The advantage of the porous-core fiber is that it is easier to manufacture than the hollow core fiber since all the holes have the same size. Through numerical calculations it has been shown that the porous-core fiber has a wider bandgap than the corresponding hollow-core fiber and lower total propagation loss. The calculations showed that 4 rings of cladding holes are required to get a wide and deep bandgap and in this bandgap the confinement loss is reduced from the material loss of 1 dB/cm to a fiber loss of 0.25 dB/cm. A 4-ring fiber with the given pitch of 250 μm could be as thin as 3 mm in diameter. This fiber is realistically manufacturable, would be half the thickness of the only previously experimentally reported THz bandgap fiber and with a loss of 0.25 dB/cm it would have 4 times lower loss.

Finally a functional THz fiber has been reported. A broadband 3-dB coupler design for THz applications has been investigated. The working principle of this device is based on mechanical down-doping of the twin cores. It has been demonstrated that bandwidths in excess of 0.8 THz are achievable at around 1.5 THz. The coupling length has also been shortened by the down-doping by a factor of two compared to a normal coupler. A figure of merit for the coupler quality has been introduced. It takes into account both bandwidth and loss. This FOM shows that a smaller bandwidth at a lower frequency is better than a large bandwidth at high frequency, because of high loss at high frequencies.

8.2 Discussion and outlook

The fabrication process is highly reproducible, and there is the possibility to manufacture optical fibers for the THz frequency range with the full range of functionalities that we see today in applications of photonic crystal fibers in the near infrared. The robustness of the fibers during subsequent processing will pave the road to functional THz fibers based devices such as couplers, Mach-Zehnder interferometers and fiber sensors, tapered fibers for field confinement and advanced dispersion management. The fibers will also become an interesting test bed for nonlinear optics in the THz range due to the long propagation distances with tight confinement of strong THz fields.

The results of the hollow core fibers shown in chapter 6 indicate that there are possibilities for lowering the propagation loss of THz fibers. Specifically designing fibers on the basis of the imaginary term of the refractive index could yield broadband low loss THz waveguides.

List of acronyms

THz	terahertz
EM	electromagnetic
PML	perfectly matched layer
PMMA	poly(methyl-methacrylate)
PCF	photonic crystal fibre
mPOF	microstructured polymer optical fiber
PBG	photonic bandgap
MPB	MIT Photonic Bands Package
LMA	Large Mode Area
SMA	Small Mode Area
THz-TDS	terahertz time-domain spectroscopy

Bibliography

[1] K. Nielsen, A. J. L. Adam, P. C. M. Planken, H. K. Rasmussen, O. Bang, P. U. Jepsen, "Bendable, low-loss topas fibers for the terahertz frequency range," Opt. Express **17**, 10, 8592-8601 (2009).

[2] K. Nielsen, H. K. Rasmussen, P. U. Jepsen, and O. Bang, "Broadband terahertz fiber directional coupler," Opt. Lett. **35**, 17, 2879-2881 (2010).

[3] K. Nielsen, H. K. Rasmussen, P. U. Jepsen, and O. Bang, "Porous core honeycomb band gap THz fiber," Opt. Lett. **00**, 00-00 (2011).

[4] P. U. Jepsen, D. G. Cooke, and M. Koch, "Terahertz spectroscopy and imaging - modern techniques and applications," Laser & Photonics Reviews DOI 10.1002/lpor. 201000011 (2010).

[5] B. E. Cole, J. B. Williams, B. T. King, M. S. Sherwin, and C. R. Stanley, "Coherent manipulation of semiconductor quantum bits with terahertz radiation," Nature **410,** 60 (2001)

[6] R. Huber, F. Tauser, A. Brodschelm, M. Bichler, G. Abstreiter, and A. Leitenstorfer, "How many-particle interactions develop after ultrafast excitation of an electron-hole plasma," Nature **414,** 286 (2001)

[7] D. G. Cooke, A. N. MacDonald, A. Hryiw, J. Wang, Q. Li, A. Meldrum, and F. A. Hegmann, "Transient terahertz conductivity in photoexcited silicon nanocrystal films," Phys. Rev. B **73,** 193311 (2006)

[8] M. C. Beard, G. M. Turner, and C. A. Schmuttenmaer, "Measuring intermolecular charge transfer via coherent generation of THz radiation," J. Phys. Chem. A **106,** 878 (2002)

[9] M. Schall, M. Walther, and P. Uhd Jepsen, "Fundamental and second-order phonon processes in CdTe and ZnTe," Phys. rev. B **64,** 094301 (2001)

[10] M. Walther, B. M. Fischer, and P. Uhd Jepsen, "Noncovalent intermolecular forces in polycrystalline and amorphous saccharides in the far infrared," Chem. Phys. **288,** 261 (2003)

[11] C. Rønne, L. Thrane, P.-O. Åstrand, A. Wallqvist, K. V. Mikkelsen, and S. R. Keiding, "Investigation of the temperature dependence of dielectric relaxation in liquid water by THz reflection spectroscopy and molecular dynamics simulation," J. Chem. Phys. 107, 5319 (1997)

[12] S. E. Whitmore, D. Wolpert, A. G. Markelz, J. R. Hillebrecht, J. Galan, and R. R. Birge, "Protein flexibility and conformational state: A comparison of collective vibrational modes of wild-type and D96N bacteriorhodopsin," Biophys. J. **85,** 1269 (2003)

[13] J. E. Bjarnason, T. L. J. Chen, A. W. M. Lee, M. A. Celis, and E. R. Brown, "Millimeter-wave, terahertz, and mid-infrared transmission through common clothing," Appl. Phys. Lett. **85,** 4, 519-521 (2004)

[14] M. Reid, and R. Fedosejevs, "Terahertz birefringence and attenuation properties of wood and paper," appl. optics, **45**, 12, 2766-2772 (2006)

[15] C. Jordens, M. Scheller, S. Wietzke, D. Romeike, C. Jansen, T. Zentgraf, K. Wiesauer, V. Reisecker, M. Koch, "Terahertz spectroscopy to study the orientation of glass fibres in reinforced plastics," composit science and techonology, **70**, 3, 472-477 (2010)

[16] J. F. Federici, B. Schulkin, F. Huang, D. Gary, R. Barat, F. Oliveira, and D. Zimdars, "THz imaging and sensing for security applications - explosives, weapons and drugs," semiconductors science and technology, **20**, 7, S266-S280 (2005)

[17] G. Gallot, S. P. Jamison, R. W. McGowan, and D. Grischkowsky, "Terahertz waveguides," J. Opt. Soc. Am. B **17,** 851 (2000)

[18] O. Mitrofanov, and J. A. Harrington, "Dielectric-lined cylindrical metallic THz waveguides: mode structure and dispersion," Opt. Express, **18,** 3, 1898-1903 (2010)

[19] R. Mendis and D. Grischkowsky, "Plastic ribbon THz waveguides," J. Appl. Phys. **88,** 4449 (2000)

[20] R. Mendis and D. Grischkowsky, "Undistorted guided-wave propagation of subpicosecond terahertz pulses," Opt. Lett. **26,** 846 (2001)

[21] R. Mendis and D. Grischkowsky, "THz interconnect with low-loss and low-group velocity dispersion," IEEE Microwave and Wireless Components Lett. **11,** 11, 444-446 (2001)

[22] K. Wang and D. M. Mittleman, "Metal wires for terahertz wave guiding," Nature **432,** 376 (2004)

[23] B. Bowden, J. A. Harrington, and O. Mitrofanov, "Silver/polystyrene-coated hollow glass waveguides for the transmission of terahertz radiation," Opt. Lett. **32,** 2945 (2007)

[24] L.-J. Chen, H.-W. Chen, T.-F. Kao, J.-Y. Lu, and C.-K. Sun, "Low-loss subwavelength plastic fiber for terahertz waveguiding," Opt. Lett. **31,** 308 (2006)

[25] S. Atakaramians, S. Afshar V., B. M. Fischer, D. Abbott, and T. M. Monro, "Porous fibers: a novel approach to low loss THz waveguides," Opt. Express **16,** 8845 (2008)

[26] A. Hassani, A. Dupuis, and M. Skorobogatiy, "Low loss porous terahertz fibers containing multiple subwavelength holes," Appl. Phys. Lett. **92,** 7, 071101 (2008)

[27] A. Dupuis, J.F. Allard, D. Morris, K. Stoffler, C. Dubois, and M. Skorobogatiy, "Fabrication and THz loss measurements of porous subwavelength fibers using a directional coupler method," Opt. Express **17,** 10, 8012-8028 (2009)

[28] S. Atakaramians, S. Afshar V., B.M. Fischer, D. Abbott, and T.M. Monro, "Low loss, low dispersion and highly birefringent terahertz porous fibers," Opt. Comm. **282,** 1, 36-38 (2009)

[29] B. Bowden, J. A. Harrington, and O. Mitrofanov, "Fabrication of terahertz hollow-glass metallic waveguides with inner dielectric coatings," J. Appl. Phys. **104**, 093110 (2008).

[30] C. S. Ponseca, Jr., R. Pobre, E. Estacio, N. Sarukura, A. Argyros, M. C. J. Large, and M. A. van Eijkelenborg, "Transmission of terahertz radiation using a microstructured polymer optical fiber," Opt. Lett. **33**, 9, 902-904 (2008).

[31] M. Goto, A. Quema, H. Takahashi, S. Ono, and N. Sarukura, "Teflon photonic crystal fiber as terahertz waveguide," Japanese J. Appl. Phys. **43,** L317 (2004)

[32] H. Han, H. Park, M. Cho, and J. Kim, "Terahertz pulse propagation in a plastic photonic crystal fiber," Appl. Phys. Lett. **80,** 2634 (2002)

[33] J. Riishede, N. A. Mortensen, and J. Lægsgaard, "A poor man's approach to modelling microstructured optical fibres," J. Opt. A, **5**, 5, 534-538 (2003)

[34] S.G. Johnson and J.D. Joannopoulos, "Block-iterative frequency-domain methods for Maxwell's equations in a planewave basis," Opt. Express **8,** 3, 173-190 (2001).

[35] A. Sengupta, A. Bandyopadhyay, B. F. Bowden, J. A. Harrington, and J. F. Federici, "Characterization of olefin copolymers using terahertz spectroscopy," Electron. Lett. **42,** 1477 (2006)

[36] G. Emiliyanov, J.B. Jensen, O. Bang, P.E. Hoiby, L.H. Pedersen, E.M. Kjær, and L. Lindvold Opt. Lett. **32**, 460 (2007)

[37] Y. S. Jin, G. J. Kim, and S. G. Jeon, "Terahertz dielectric properties of polymers," J. Korean phys. soc.,**49**, 2, 513-517 (2006)

[38] M. Naftaly and R. E. Miles, "Terahertz time-domain spectroscopy of silicate glasses and the relationship to material properties," J. Appl. Phys. **102,** 043517 (2007)

[39] S. P. Jamison, R. W. McGowan, and D. Grischkowsky, "Single-mode waveguide propagation and reshaping of sub-ps terahertz pulses in sapphire fibers," Appl. Phys. Lett. **76,** 1987 (2000)

[40] T. A. Birks, J. C. Knight, and P. St. J. Russell, "Endlessly single-mode photonic crystal fiber," Opt. Lett. **22,** 961 (1997)

[41] Y. F. Geng, X. L. Tan, P. Wang, and J. Q. Yao, "Transmission loss and dispersion in plastic terahertz photonic band-gap fibers," Appl. Phys. B **91,** 333 (2008)

[42] L. Vincetti, "Hollow core photonic band gap fiber for thz applications," Microwave Technol. Lett. **51** 1711-1714 (2009).

[43] A. Hassani, A. Dupuis, and M. Skorobogatiy, "Porous polymer fibers for low-loss terahertz guiding," Opt. Express **16,** 6340 (2008)

[44] J. Y. Lu, C. P. Yu, H. C. Chang, H. W. Chen, Y. T. Li, C. L. Pan, and C. K, Sun, "Terahertz air-core microstructure fiber," Appl. Phys. Lett. **92**, 064105 (2008).

[45] R. F. Cregan, B. J. Mangan, J. C. Knight, T. A. Birks, P. St. J. Russell, P. J. Roberts, and D. C. Allan, "Single-mode photonic bang gap guidance of light in air," Science **285**, 5433, 1537-1539 (1999).

[46] M. Large, L. Poladian, G. Barton, and M. A. van Ejkelenborg, *Microstructured Polymer Optical Fibres,* Springer Science+Business Media (2005)

[47] James E. Mark, *Polymer data handbook,* Oxford Univeristy Press, (1999)

[48] TOPAS Advanced polymers webpage, `http://www.topas.com/tds_8007f_04_e-2.pdf`

[49] M. F. Ashby, and D. R. H. Jones, *Engineering Materials 1,* Butterworth-Heinemann (1996)

[50] S. L. Dexheimer, *Terahertz Spectroscopy: Principles and applications,* CRC Press (2008)

[51] M. D. Nielsen and N. A. Mortensen, "Photonic crystal fibers design based on the v-parameter," Opt. Lett. **11,** 2762 (2003)

[52] A. J. L. Adam, J. M. Brok, M. A. Seo, K. J. Ahn, D. S. Kim, J. H. Kang, Q. H. Park, M. Nagel, and P. C. M. Planken, "Advanced terahertz electric near-field measurements at sub-wavelength diameter metallic apertures," Opt. Express **16,** 7407 (2008)

[53] N.A. Mortensen and J.R. Folkenberg, "Low-loss criterion and effective area considerations for photonic crystal fibres ," J. Opt. A: Pure Appl. Opt. **5**, 3, 163-167 (2003)

[54] J. M. Pottage, D. M. Bird, T. A. Birks, J. C. Knight, P. J. Roberts, and P. St. J. Russell, "Robust photonic band gaps for hollow core guidance in PCF made from high index glass," Opt. Express, **11**, 22, 2854-2861 (2003)

[55] A. Bitzer, A. Ortner, and M. Walther, "Terahertz near-field microscopy with subwavelength spatial resolution based on photoconductive antennas," Applied Optics, **49,** 19, E1-E6 (2010)

[56] A. W. Snyder, J. Love, *O*ptical Waveguide Theory, Kluwer Academic Publishers (2000).

[57] N. A. Issa, A. Argyros, M. A. van Eijkelenborg, and J. Zagari, "Identifying hollow waveguide guidance in air-cored microstructured optical fibres," Opt. Express, **11**, 9, 996-1001 (2003)

[58] M. Miyagi, and S. Kawakami, "Design Theory of dielectric-coated circular metallic waveguides for infrared transmission," J. Lighwave Tech., **LT-2,** 2, 116-126 (1984)

[59] P. Kristensen, T. B. Nielsen, J. Riishede, and J. Lægsgaard, "Light guiding in microstructures of purely imaginary refractive index contrast," Photonics and nanostructures-fundamentals and applications, **3,** 1, 1-9 (2005)

[60] J. Broeng, S. E. Barkou, A. Bjarklev, J. C. Knight, T. A. Birks, and P. S. Russell, "Highly increased photonic band gaps in silica/air structures," Opt. Communications **156**, 4-6 (1998).

[61] J. Lægsgaard, O. Bang, and A. Bjarklev, "Photonic crystal fiber design for broadband directional coupling," Opt. Lett. **29,** 21, 2473-2475 (2004)